Journal of Atmospheric Chemistry **37:** 245–282, 2000.

Fast-J: Accurate Simulation of In- and Below-Cloud Photolysis in Tropospheric Chemical Models

OLIVER WILD*, XIN ZHU and MICHAEL J. PRATHER
Earth System Science, University of California, Irvine, CA 92697, U.S.A.

(Received: 16 December 1999; accepted: 30 March 2000)

Abstract. Photolysis rates in the troposphere are greatly affected by the presence of cloud and aerosol layers. Yet, the spatial variability of these layers along with the difficulty of multiple-scattering calculations for large particles makes their inclusion in 3-D chemical transport models computationally very expensive. This study presents a flexible and accurate photolysis scheme, Fast-J, which calculates photolysis rates in the presence of an arbitrary mix of cloud and aerosol layers. The algorithm is sufficiently fast to allow the scheme to be incorporated into 3-D global chemical transport models and have photolysis rates updated hourly. It enables tropospheric chemistry simulations to include directly the physical properties of the scattering and absorbing particles in the column, including the full, untruncated scattering phase function and the total, uncorrected optical depth. The Fast-J scheme is compared with earlier methods that have been used in 3-D models to parameterize the effects of clouds on photolysis rates. The impact of Fast-J on tropospheric ozone chemistry is demonstrated with the UCI tropospheric CTM.

Key words: photolysis rates, tropospheric chemistry, chemical transport modelling.

1. Introduction

Throughout much of the troposphere, clouds and aerosols alter the photolysis rates that drive atmospheric chemistry. In the stratosphere the effects of tropospheric clouds can be treated reasonably by selecting the height and albedo of the lower optical surface, whereas in the troposphere much of the chemistry occurs within cloud-aerosol layers, or even below them. In developing global tropospheric chemistry-transport models (CTMs), it is necessary to simulate the enhanced photochemical rates above and in the upper levels of clouds as well as the reduced rates below optically thick clouds and absorbing aerosols (e.g., Logan *et al.*, 1981; Madronich, 1987). Such previous work has demonstrated the capability of modeling photochemistry for at least horizontally homogeneous clouds and aerosol layers, yet the computational demands of three-dimensional CTMs has precluded the practical inclusion of these numerically accurate solutions. The number of degrees of freedom, such as cloud height and absorbing aerosol, prevent a simple parametric fit of these accurate schemes in terms of a few variables. This paper presents a

* Now at the Frontier Research System for Global Change, Tokyo,
e-mail: oliver@frontier.esto.or.jp

new algorithm, Fast-J, to calculate photolysis rates throughout the troposphere in the presence of an arbitrary mix of cloud and aerosol layers, given their optical properties: Extinction optical depth, single scattering albedo, and scattering phase function. This Fast-J algorithm is demonstrated to be accurate compared to the more detailed photolysis codes, and it is so efficient that its incorporation in 3-D CTMs gives only modest (about 10%) increase in computational time. Fast-J enables simulations of global tropospheric photochemistry to include directly the physical properties of the scattering and absorbing particles in the column.

The development of accurate radiative transfer models for visible and ultraviolet sunlight with wavelengths from 180 to 800 nm is necessary for stratospheric and tropospheric chemistry models. While a number of these codes treating multiple scattering are available, e.g., the Gaussian quadrature and integral-equation methods of Chandrasekhar (1960) and the subsequent second-order finite-difference approach of Feautrier (1964), and have been applied to inhomogeneous, layered atmospheres (e.g., Auer, 1967; Stamnes *et al.*, 1988; Anderson *et al.*, 1995; Liao *et al.*, 1999), these methods have been too computationally intensive for ready use in large CTMs. These models are more commonly restricted to using two-stream approximations (Isaksen *et al.*, 1977; Hough, 1988; Roelofs and Lelieveld, 1995) rather than more detailed multiple-stream approaches. The accuracy of the two-stream approach has been improved by applying a delta-scaling approximation to correct the calculated irradiances in strongly forward scattering conditions, e.g., the delta-Eddington method of Joseph *et al.*, (1976), but recent studies have highlighted problems with these corrections (Zeng *et al.*, 1996; Boucher *et al.*, 1998). Kylling *et al.* (1995) describe a more reliable two-stream algorithm based on a reduced form of the multiple-stream discrete-ordinate approach; while this scheme is an improvement over earlier methods, it remains relatively computationally expensive. Early Feautrier-based (1964) multiple-stream methods were fast and accurate for Rayleigh/isotropic scattering (Prather, 1974) but unable to handle strongly forward peaked scattering typical of large particles without the delta-M approach of re-adjusting the optical depth (Wiscombe, 1977).

One of the earlier efforts at averaging tropospheric photochemistry over a climatological range of cloud cover (Logan *et al.*, 1981) included clouds, but only as fully reflecting layers. That study looked at the role of background aerosols on photolysis rates and concluded that the most important correction was the inclusion of a 'clean-air' optical depth of 0.02 of fully absorbing aerosol at 310 nm. These early approaches ignore the enhancement of scattered light in the upper parts of clouds and aerosol layers and the diminished, but still non-negligible transmission of sunlight below clouds with extinction optical depths much greater than 1 (Jacob *et al.*, 1989; Madronich, 1987). Another simple, but effective, technique has been to apply a correction factor, scaling clear-sky photolysis rates above, inside and below clouds, dependent on the solar zenith angle and optical depth (Chang *et al.*, 1987; Muller and Brasseur, 1995; Brasseur *et al.*, 1998). This technique allows the spatial and temporal variability of cloud layers to affect calculated photolysis

rates directly, but it remains a first-order approach, and there are many conditions under which the approximations are inappropriate, for example in the presence of multiple layers of cloud or aerosol, or where the particles have different optical properties.

Currently, in the absence of computationally-efficient photolysis schemes suitable for CTMs, many modelling studies rely on pre-calculation of photolysis rates off-line for a variety of different solar zenith angles, and then tabulation for later interpolation during the model run (Brasseur *et al.*, 1998; Berntsen and Isaksen, 1997; Kraus *et al.*, 1996). This removes the need for calculation during the run, and allows the use of a more detailed photolysis scheme than could be included in the model. However, pre-calculation requires one or more standard atmospheres, and therefore prevents interactive inclusion of the effects of the modelled ozone column, or of highly variable cloud or aerosol loadings. The effects of cloud or aerosol may be included in these tables based on parameterizations of cloud cover at pre-defined optical depths and locations (Berntsen and Isaksen, 1997), but the user is then restricted to a few pre-defined scenarios. A more efficient method has recently been proposed by Landgraf and Crutzen (1998), using pre-calculated tables of photolysis rate constants for a purely absorbing atmosphere, and applying a correction factor at run-time with a radiative transfer code to take account of molecular, aerosol and cloud scattering effects. This method addresses some of the problems with previous schemes, providing a better simulation of the variability of photolysis rates due to clouds and aerosol, but it remains reliant on detailed parameterizations.

The Fast-J photolysis scheme has been developed for flexibility as well as accuracy. It uses directly the physical properties of the scattering and absorbing particles in the atmosphere as calculated by a model or as specified in a climatology. The scheme is computationally quick and can be run on-line in a CTM without a significant increase in computational time. In Section 2 we highlight the key features of the scheme, and describe how it is implemented in the UCI CTM. We review the sensitivity of photolysis rates to the distributions and phase functions for atmospheric aerosols and clouds in Section 3. Section 4 describes some applications of the scheme, and demonstrates the importance of cloud and aerosol scattering for tropospheric chemistry.

2. Description and Implementation

2.1. APPROXIMATING MULTIPLE SCATTERING WITH LARGE PARTICLES

Exact solutions to the multiple-scattering problem in plane parallel or quasi-spherical atmospheres are available in a limited number of cases through analytic forms (e.g., Chandrasekhar, 1960). Numerically accurate solution of the radiative transfer equation – as resolved at a finite number of Gaussian quadrature points – can also be found (e.g., Auer, 1967; Stamnes *et al.*, 1988). A new anisotropic

method following Feautrier (1964) based on finite-difference approximation to the differential equations in optical depth is given in Appendix A.

Following Chandrasekhar, these numerical solutions generally rely on expansion of the scattering phase function in Legendre polynomials. The simplest case for aerosol and cloud particles involves use of only the first asymmetric term with coefficient $\omega^1 = 3\,\overline{\cos}$, where $\overline{\cos}$ is the average of the cosine of the scattering angle weighted by the phase function. Other approaches take the Henyey–Greenstein phase function (Henyey and Greenstein, 1941), which has a simple and rapidly converging expansion for typical asymmetry factors, $g = \overline{\cos}$. For large aerosols and cloud droplets, however, the scattering phase function is strongly forward peaked and not easily represented by a truncated Legendre expansion (e.g., van de Hulst, 1981). In this case the forward, coronal scattering of the sunlight is ignored; this truncated phase function is refitted to the Legendre polynomials, and the effective optical depth is reduced (e.g., Wiscombe, 1977). Such an approach has been used by earlier versions of this photolysis code when modeling photochemistry in and below clouds (Jacob *et al.*, 1989), and it required reduction of the scattering optical depths for cloud droplets by almost a factor of two.

In contrast, the Fast-J algorithm is based on a Legendre expansion of the exact scattering phase function, and thus no adjustment to optical depth or extinction coefficient is needed. A series of numerical tests, including expansion of forward-peaked phase functions to 160 terms, demonstrates that truncation of the Legendre expansion at 8 terms gives an accurate calculation of the mean specific intensity of the radiation field although the specific intensity field itself (a function of zenith and azimuth angles) is noisy and not even positive definite; see Appendix B. The photolytic intensity (sometimes called 'actinic flux') is the sum of the direct solar flux (perpendicular to the beam, not cosine weighted) plus the 4π-steradian integrated mean specific intensity (sometimes called 'radiance', see Chapter 2 of Goody and Yung (1989)).

In summary, Fast-J solves the 8-stream multiple scattering problem, using the exact scattering phase function and optical depths, and provides photolytic intensities accurate typically to better than 3%, with worst case errors of no more 10% over a wide range of atmospheric conditions. No special approximations are needed to treat strongly forward-peaked phase functions. Fast-J incidentally calculates the divergence of the total flux (cosine-weighted) throughout the atmosphere, and can thus be used to calculate accurately short-wave heating rates in the presence of clouds, aerosols and absorbers with little additional effort.

2.2. OPTIMIZING INTEGRALS OVER WAVELENGTH

In the majority of photolysis schemes, the solar spectrum is divided up into a large number of wavelength bins, the mean photolytic intensity is calculated for each bin, and the contribution to the total photolysis rate is summed, given the mean absorption cross-section for each species over each bin. Absorption cross-sections for use

in chemical models are often tabulated in the range 116 to 730 nm in 171 intervals (WMO, 1986; DeMore *et al.*, 1997), of which about 125, with wavelengths greater than 175 nm, are important for the stratosphere and troposphere (e.g., Hough, 1988). The need to calculate the mean intensity at so many wavelengths provides one of the most serious computational constraints on the speed of such schemes.

The integration over wavelength is just a form of quadrature, and the Fast-J algorithm derives an optimal quadrature through an objective analysis of the location of these wavelength bins by minimizing the error in key J-values over a range of atmospheric conditions (e.g., clear sky, clouds, solar zenith angles). It is found that 7 wavelength bins of varying widths covering the wavelengths from 289 to 850 nm can reproduce a standard, high-resolution (i.e., 1 nm) calculation of J's to about 3%, see Appendix C.

In the visible and near-UV region (289–850 nm) cross sections for species of photochemical interest are taken from IUPAC V (Atkinson *et al.*, 1997) and JPL (DeMore *et al.*, 1997) recommendations, and have been reapportioned into the 7 wavelength bins used by Fast-J by interpolating onto a 10 cm^{-1} grid, weighting by the solar flux (LOWTRAN7, Rev. 4.2 (1 Feb. '92); Thekeakara, 1974), and then lumping into the appropriate bin. The cross-sections for O_3 and the quantum yield of $O(^1D)$ have been tabulated at 3 temperatures, and values at each atmospheric level are linearly interpolated. Fast-J computes the photolytic intensity (e.g., photons cm^{-2} s^{-1}) in each of the 7 wavelength bins at any requested levels in the atmosphere. The photolysis rate, J_X, for any species X is then calculated by summing the product of photolytic intensity and mean cross section over the 7 bins. It is critical that the mean cross section for X in each bin be computed by averaging the cross section weighted by the solar flux over that interval. Fast-J provides precalculated mean cross sections for many species at 2 temperatures and interpolates local cross sections linearly with temperature. Pressure-dependent cross sections are not used in the standard version, but could be derived by suitable weighting of photolytic factors across wavelengths (Cameron-Smith, 2000).

A small but significant flux of sunlight reaches the upper tropical troposphere in the Herzberg continuum (200–215 nm). Photolysis at these wavelengths can be important for species that are otherwise inert in the troposphere. For example, photolysis of O_2 produces O_3 in the upper tropical troposphere at rates on the order of ppb/day, and similar loss of the halons 1211 and 2402 in the troposphere is a major factor in their atmospheric lifetimes. This short-wavelength radiation will interact with high altitude clouds and aerosols in the tropics, enhancing the photolysis rates and thus we wish to include it in Fast-J. Unfortunately, the optical depths due to overhead O_2 and O_3 in the troposphere are large (each greater than 3), and the effective wavelength of the transmitted sunlight shifts with altitude. While no generalizable wavelength bins can be used for Fast-J, a simple fitting of the J-values for several key species allows the scattering code of Fast-J to be applied to the upper tropical troposphere. In the Herzberg continuum the effective absorption cross sections for O_2 and O_3 are 8.15×10^{-24} cm^2 and 4.40×10^{-19} cm^2,

respectively. An attenuation factor is derived from the effective cross sections and the O_2 and O_3 concentrations for each layer, and this is used to scale 'top-of-the-atmosphere' J-values in the 12 to 18 km altitude range, taking into account the effects of scattering. 'Top-of-the-atmosphere' pseudo J-values for O_2, halon-1211, and halon-2402 are 1.67×10^{-10}, 2.76×10^{-5} and 2.75×10^{-5} s^{-1}, respectively. Note that J_{O_3} is not included since the longer wavelengths (greater than 289 nm) dominate and that J_{O_2} is not consistent with the absorption cross section.

2.3. CTM LAYERS AND FAST-J LEVELS

The Fast-J photolysis scheme has been implemented in the UCI CTM, an off-line 3-D global model based on the GISS CTM of Prather *et al.* (1987) and including a detailed tropospheric chemistry (Wild and Prather, 2000). The CTM uses meteorological fields from a $4^\circ \times 5^\circ$ version of the GISS II′ GCM (Rind and Lerner, 1996), with either 9 or 23 levels in the vertical, which are available at 3-hour intervals. The Fast-J scheme uses the surface albedo and the mean cloud optical depth in each CTM layer as reported from the 3-hour meteorological fields. A background climatology of zonal mean profiles of monthly ozone and temperature (based on the Models and Measurements Workshop, see Prather and Remsberg (1993)) is included with Fast-J so that a complete ozone profile can be specified where the CTM does not calculate one.

Photolysis rates are required at the centres of CTM layers, and these pressure levels, together with the boundaries between layers, define the basic level structure used in the Fast-J scheme. The optical depth in each model layer is mapped onto the Fast-J levels by apportioning it equally between the levels on either side of the centre of the CTM layer. The ozone and air mass of these levels are similarly defined, and the attenuation of the direct solar beam is then calculated at each Fast-J level, correcting for spherical geometry. The coefficients of the scattering phase function at the levels corresponding to the centre of model layers are calculated directly from the optical properties of the layer; the coefficients at the levels corresponding to the boundaries are calculated by an optical depth-weighted interpolation of the values at the mid-points, ensuring that the column-integrated scattering is maintained at the value of the original CTM column. Where the optical thickness of one of these Fast-J levels exceeds a predetermined threshold, additional levels are inserted equidistantly in optical depth. Single-scattering albedos and phase functions are interpolated as before to ensure conserved optical column properties, and the attenuation of the solar beam is interpolated logarithmically. Currently a threshold optical thickness of 1.0 is used, with a higher threshold of 0.1 in the uppermost optical depth to provide a better treatment of the scattering when the direct beam is dominant. The finite-difference solution to the equation of radiative transfer is solved for the mean photolytic intensity at every odd point in the Fast-J levels (see Appendix A), which includes the mid-point of each CTM layer.

2.4. TESTS AND COMPUTATIONAL COSTS

Calculation of photolysis rates with the conditions defined by the IPCC Photochemical Model Intercomparison (Olsen *et al.*, 1997) produces results in close agreement with those of other models. The clear-sky photolysis rates for NO_2 are about 5% larger than the mean values tabulated there, in close agreement with the other multi-stream methods, and reflecting the importance of multiple scattering for those molecules where absorption cross-sections are above 300 nm, a feature not well reproduced in the two-stream approximations in common use. This comparison was performed with the cross-sections available in 1995/6, before recent changes in the recommended ozone cross sections (DeMore *et al.*, 1997).

In Fast-J, the specific intensity of multiply scattered light is solved at 8 Gauss points (4 upward and 4 downward) and then integrated over 4π steradians to calculate the mean intensity. For each wavelength the absorption cross-sections are multiplied by the flux as the final step in the calculation, and hence the CPU time required by the scheme is relatively insensitive to the number of species photolysis rates are calculated for.

In the UCI CTM, the tropospheric chemistry scheme typically accounts for 66% of the total CPU time, and the transport scheme for about 20%. The chemical scheme included in the CTM involves 35 chemical species, 27 of which are solved for directly with an implicit integration scheme using Newton–Raphson iteration. Full calculation of photolysis rates at every grid point at every chemical time-step (hourly) takes one tenth of the computational time required for the chemistry, just 7% of the total CPU time.

Within Fast-J, 80% of the time is taken solving the scattering problem, and most of the remaining 20% is spent setting up the level scheme and calculating the column properties. The overhead for setting up the levels would still be required for a simple two-stream photolysis code, and hence it is estimated that Fast-J takes about 4–5 times as long to run; however, this difference only accounts for about 5% of the total CPU time for the CTM. A discrete-ordinate code, DISORT, (Stamnes *et al.*, 1988) run in eight-stream mode takes 20–30 times as long, an unacceptable overhead for a CTM which would more than double the total CPU time.

3. Atmospheric Clouds and Aerosol

Measurements from the International Satellite Cloud Climatology Project (ISCCP) indicate a global annual average cloud optical depth of about 5, though the optical depth varies greatly with time and location (Rossow and Schiffer, 1991). Mineral aerosols have an global mean optical depth of about 0.023 (Schimel *et al.*, 1996), but exceeding 0.3 in Northern Hemisphere desert regions in the summer (Tegen and Fung, 1995). Carbonaceous aerosols from natural sources have a global mean optical depth of 0.011 (Schimel *et al.*, 1996), and the optical depth of soot from anthropogenic sources is about 0.003, but both are highly variable, and are concentrated over continental source regions (Liousse *et al.*, 1996). Sulphate aerosols

from industrial and biomass burning sources have mean optical depths of about 0.019 and 0.017, respectively, while sulphate aerosol from natural sources has a mean optical depth of about 0.014 (Schimel *et al.*, 1996). The total global mean optical depth from natural and anthropogenic aerosol is about 0.1.

These scattering particles are present in the atmosphere in a wide range of sizes, and it is primarily the size that determines the scattering properties. Particles whose circumference ($2\pi r$) is much less than the wavelength of light tend to scatter more isotropically and have scattering efficiencies (Q) that are much greater in the ultraviolet than visible spectrum. Larger particles scatter light in the forward direction, with very large particles, like cloud droplets, having as much as half of their scattering in a strong forward peak within a few degrees of the original beam (van de Hulst, 1981). These large particles have scattering efficiencies independent of wavelength in the ultraviolet and visible spectrum and hence appear white or gray. Haze or fog in the lower atmosphere generally contains much smaller droplets than clouds, and hence tends to scatter more isotropically. Sulphate aerosol in the lower stratosphere has a circumference typical of visible light and thus is forward scattering but with an easily resolved phase function. Ice clouds, with large (50 μm) multi-edged crystals, have a phase function distinctly different from Mie-theory water clouds (Mishchenko *et al.*, 1996). Black carbon (soot) particles are primarily important in the atmosphere as absorbers. Other particles such as dust (Tegen and Fung, 1995), sea salt (Quinn *et al.*, 1996) and biogenic aerosols (Penner *et al.*, 1992) have unique scattering properties. Further, internal mixes of these aerosol types will produce scattering that may not be readily represented by an external mix of the optical properties of the individual components.

Fast-J has included the scattering phase functions for a wide variety of atmospheric aerosols. With the exception of ice clouds (Mishchenko *et al.*, 1996) all of these scattering function are calculated with Mie theory. In the CTM applications included here we have made some simplifying assumptions. Mature water clouds typically have droplets of 5–10 μm radius; as the scattering properties of particles in this size range are similar, the phase function for a cloud with mode radius of 8 μm has been adopted whenever a cloud optical depth is diagnosed in the meteorological data. However, for temperatures less than 233 K, the clouds are assumed to consist of irregular-ice crystals. A simple profile of absorbing, black-carbon aerosol has been used with uniform distribution between the surface and 10 km and total optical depth of 0.001. Such low values represent relatively clean conditions and have little effect on photolysis rates (see Appendix B). It is expected that in many CTM simulations Fast-J will be more interactive, taking the aerosol optical depths and scattering properties (including internal mixtures) directly from the real-time calculations.

4. Differing Cloud Treatments – Intercomparison Studies

Two key photolysis rates control much of tropospheric chemistry:

$$O_3 \longrightarrow O_2 + O(^1D) \qquad (J_{O_3/^1D})$$

$$NO_2 \longrightarrow NO + O(^3P)\,. \qquad (J_{NO_2})$$

Photolysis of O_3 to produce $O(^1D)$ occurs primarily about 310 nm and is therefore strongly dependent on Rayleigh scattering and stratospheric ozone column. $J_{O_3/^1D}$ falls off rapidly with zenith angle and is also controlled by tropospheric ozone. Photolysis of NO_2 occurs primarily about 380 nm and is thus independent of ozone absorption and less affected by Rayleigh scattering.

4.1. CLOUD TREATMENTS

Photolysis rates calculated with the full scattering/absorption treatment of Fast-J are compared with clear-sky values and with those calculated using two parameterized cloud schemes in common usage for tropospheric CTMs, the Logan (Logan *et al.*, 1981) and Chang (Chang *et al.*, 1987) techniques.

In the Logan scheme, clouds are represented by totally reflecting Lambertian surfaces. Cloud optical depths supplied from the meteorological data are used to define the cloud top level; for optically thin clouds, with optical depth less than 4, clear-sky values are used. This is similar to the technique of Logan *et al.* (1981), where the photolysis rates used were a linear combination of those calculated with clear sky and with an opaque cloud layer.

In the Chang scheme, the clear-sky photolysis rates are multiplied by a correction factor to account for a single layer of clouds, similar to the technique used in the Regional Acid Deposition Model of Chang *et al.* (1987). This factor is dependent on the solar zenith angle, the cloud optical depth, and whether the level considered is above, in or below the cloud. As no information on cloud fractional coverage is available for our CTM, clouds are assumed to cover the whole $4^\circ \times 5^\circ$ grid box uniformly. For thin clouds with optical depth less than 5, clear-sky values are used.

The assumption of uniform cloud cover may introduce a bias to the calculated photolysis rates compared to a weighted average of cloud-covered and cloudless values. However, with partly cloudy skies there is a large added uncertainty in how to calculate and average radical chemistry under clear and cloudy conditions. As no formalism for treating these variations within a grid cell currently exists in chemical models, the simplest assumption of uniform cloud cover is made for these studies.

4.2. ONE-DIMENSIONAL TEST CASE

A simple, comparative study of the characteristics of the different schemes has been performed by calculating the photolysis rates for NO_2 at solar zenith angles

of 0° and 60° with a cloud of fixed total optical depth distributed in different layers within the troposphere. The atmosphere used is based on equatorial equinoctial conditions, and the cloud of optical depth 15 is: (i) placed in the mid-troposphere (400–550 mb), (ii) spread evenly throughout the troposphere (150–850 mb), and (iii) placed in two layers in the upper (150–250 mb) and lower (750–850 mb) troposphere with optical depths 5 and 10, respectively. The tropospheric profiles of J_{NO_2} are shown in Figure 1, where the grey blocks on the left represent the location and optical depth of the clouds.

For the mid-troposphere cloud (i), J_{NO_2} is enhanced above and throughout much of the cloud, with reductions below the cloud. At larger zenith angles, the reductions below the cloud are more substantial, as expected. The Chang and Fast-J cloud schemes produce very similar results, though the Chang technique shows a smaller in-cloud enhancement and greater above-cloud enhancement for an overhead sun. The reduction in enhancement with height above the cloud top is not reproduced with the Chang technique, but in other respects the technique gives good results. The Logan technique cuts off photolysis at the top of the cloud. While overestimating the photolysis rates above the cloud, it underestimates those below, but it may still give reasonable average rates with a suitable selection of clear-sky fraction.

For the deep cloud (ii), the influence of a full scattering treatment is more evident. Whereas in the Chang technique a constant in-cloud scaling factor is assumed, Fast-J captures the full variability of the photolysis rate throughout the cloud. At both zenith angles, compared with the Chang technique, Fast-J gives larger rates at the top of the cloud, and smaller at the base. This scenario, with a small cloud optical depth spread uniformly through the troposphere, fails to trigger the cloud treatment in our implementation of the Logan technique.

With two layers of cloud (iii), the benefits of a full scattering calculation are again clear. In our application of the Chang technique, we assume that the layers between the clouds are also in cloud, and the profile is therefore the same as that for the deep cloud. With Fast-J, in addition to capturing the enhancement in the upper cloud, the enhancements brought about by internal reflections between the cloud layers are also reproduced. This internal reflection effect is much reduced at higher zenith angles, and the Fast-J and Chang treatments agree better at 60°. Compared with the uniformly distributed cloud, there are considerably greater photolysis rates in the lower troposphere, a feature not reproduced by the Chang technique.

Calculating photolysis rates for the same cloud scenarios with the DISORT code run in eight-stream mode (not shown), the differences are below 1% in most cases, and are maintained below 3% in the worst case over thick cloud decks. These differences are principally due to the greater truncation of the phase function in Fast-J, an error term which has already been assessed in the design of the algorithm, see Appendix B.

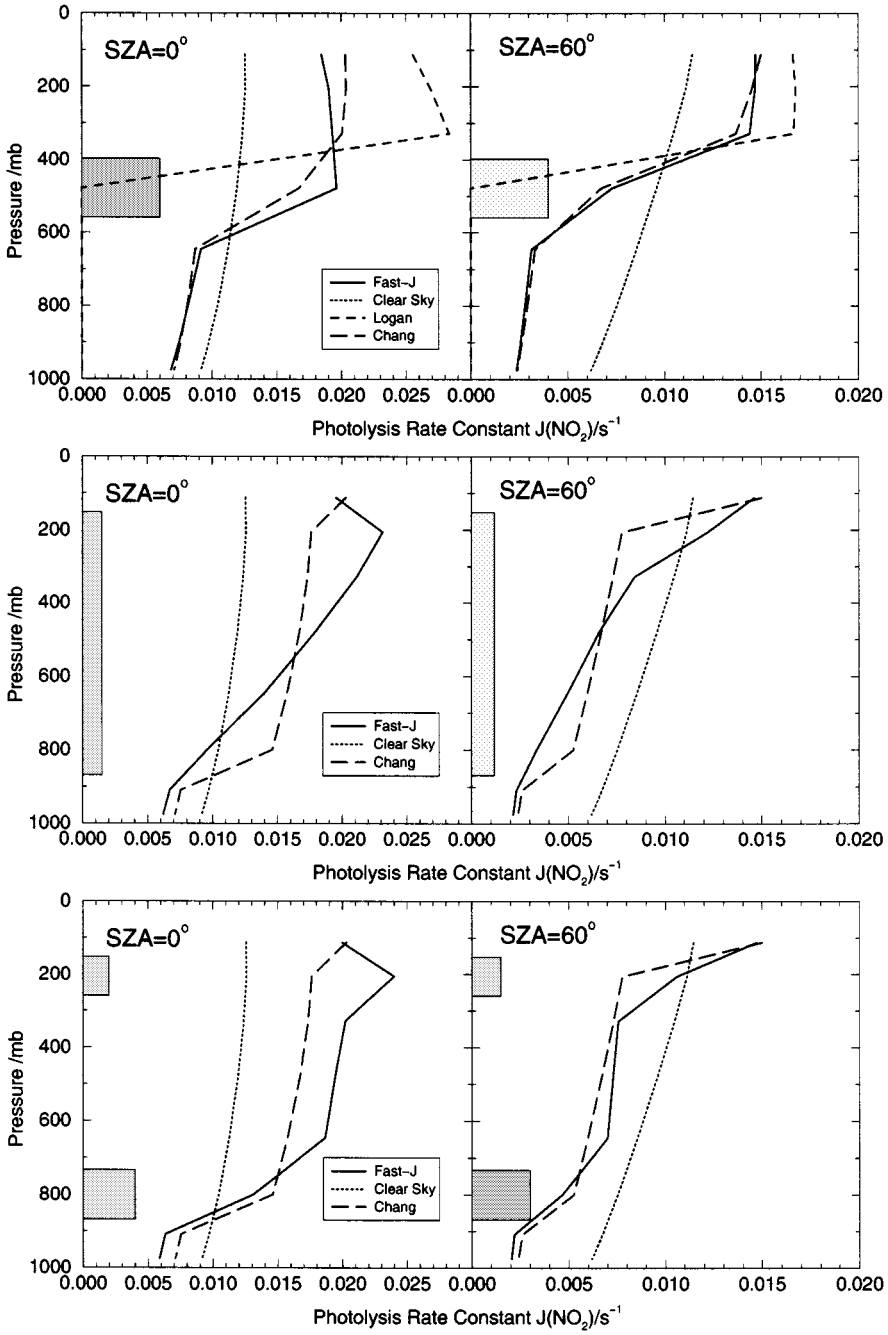

Figure 1. Photolysis rate J_{NO_2} calculated for solar zenith angles of 0° and 60° in the presence of a cloud of optical depth 15 placed (i) in the mid-troposphere (400–550 mb), (ii) throughout the troposphere (150–850 mb), and (iii) in two layers, in the upper troposphere (150–250 mb, optical depth 5) and the lower troposphere (750–850 mb, optical depth 10). The grey blocks to the left of the graphs illustrate the size and extent of the clouds. Results show the impact of different treatments of photolysis: clear-sky, Logan method, Chang method, and Fast-J. The ozone column is 255 DU, and surface albedo 0.05.

4.3. CTM INTEGRATED *J*-VALUES

The integrated effect of these different photolysis schemes over a wide range of global conditions is studied with the UCI CTM. The zonally and diurnally averaged photolysis rates, $J_{O_3/^1D}$ and J_{NO_2}, for the third week of September are calculated for a range of latitudes and shown in Figure 2. Remarkably, with this averaging the differences between the three cloud schemes are minimal, especially for the global average. As expected, all three lead to a net reduction in the photolysis rates at the surface compared to the clear-sky calculation and to a net enhancement in the upper troposphere. Comparing Fast-J with clear sky, the overall effect of clouds is global mean enhancements of 10% (J_{NO_2}) and 8% ($J_{O_3/^1D}$) in the upper troposphere, and reductions of 11% and 7% at the surface. At polar latitudes accurate treatment of clouds is less important due to lighter cloud cover; whereas in the tropics the effects may be large with enhancements averaging 14% (J_{NO_2}) and 10% ($J_{O_3/^1D}$) in the upper troposphere.

In the presence of clouds, the Logan technique gives enhancements to photolysis rates that are similar to Fast-J in the mid-troposphere but over-emphasize the effects of clouds in the upper troposphere and close to the surface. The greatest overestimates for J_{NO_2} and $J_{O_3/^1D}$ appear at about 16 km in tropical regions and 12 km at mid-latitudes, reflecting the model level immediately above the highest clouds. The Chang technique has closer agreement with Fast-J, but underestimates photolysis rates in the mid-troposphere for the tropics and mid-latitudes. The difference between these two techniques is less at higher latitudes where the vertical extent of clouds is smaller and the multiple-layering of clouds is less common. Only at the surface (and at the highest altitudes) do the Chang rates exceed those from Fast-J, a consequence of the assumption that the rates above and below clouds are proportional to those in clear-sky conditions. The greatest impact of cloud scattering on tropospheric chemistry will lie with the overall shift of photolysis to higher altitudes, as seen in the OH climatology of Spivakovksy *et al.* (2000), and further with the differential shift of the J_{NO_2} and $J_{O_3/^1D}$ photolysis rates.

4.4. GLOBAL CHEMISTRY

The primary interest in accurate modeling of photochemistry in the presence of cloud and aerosol layers is to improve our simulation of tropospheric ozone and oxidation processes (i.e., the hydroxyl radical, OH). With clouds and aerosols there is a high degree of spatial and temporal variability in photolysis rates that may be expected to correlate with the variations in O_3, NO_x ($= NO + NO_2$), and reactive hydrocarbons. Tropospheric chemistry is not therefore easily represented by average photolysis rates as analyzed in the previous section, and we present results from a full-chemistry run of the UCI CTM using different treatments for photolysis. A slowly changing, multi-year simulation using Fast-J is used to initialize the CTM on 1 September. Separate three-week runs with different photolysis treatments (Fast-J, clear-sky, Logan, Chang) are made, with results averaged over

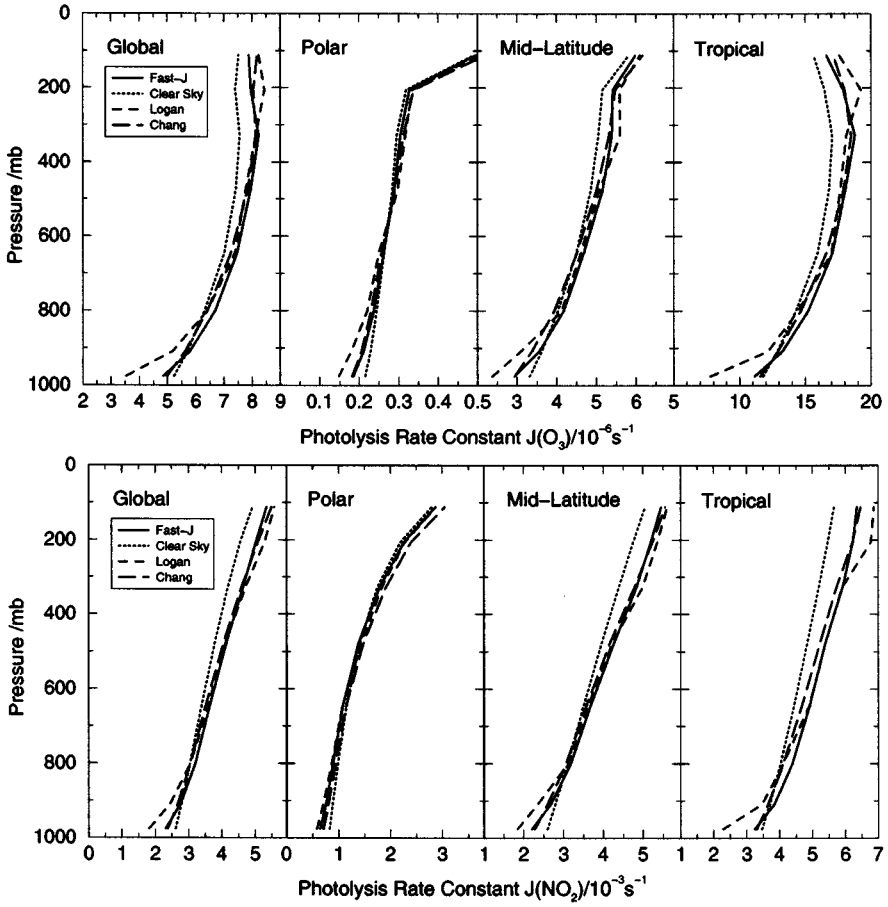

Figure 2. Zonally and diurnally averaged profiles of $J_{O_3/^1D}$ and J_{NO_2} calculated in the CTM for the third week of September. *J*-values are averaged over the globe and 3 latitude bands: Polar (68° N–90° N), Mid-latitude (40° N–60° N) and Tropical (24° S–24° N). Results are shown for clear-sky, Logan and Chang methods, and Fast-J.

the third week of September. Global mean profiles of net photochemical tendencies for O_3 and CH_4 are presented in Figure 3. The tendency for CH_4 is effectively its oxidation rate and hence a surrogate for OH.

The largest overall systematic effect of the different cloud treatments is seen in the mid-troposphere, where Fast-J shows largest enhancements in CH_4 oxidation (5% above clear-sky). This increase is driven primarily through $J_{O_3/^1D}$. At the surface all cloud methods have slower CH_4 oxidation than clear sky as expected. The globally integrated methane loss for the period is 3% greater with Fast-J than in clear-sky conditions, 1% greater with the Chang technique, and 7% less with the Logan technique. This effect is also seen in the shift in OH predicted with cloud climatology in Spivakovsky *et al.* (2000).

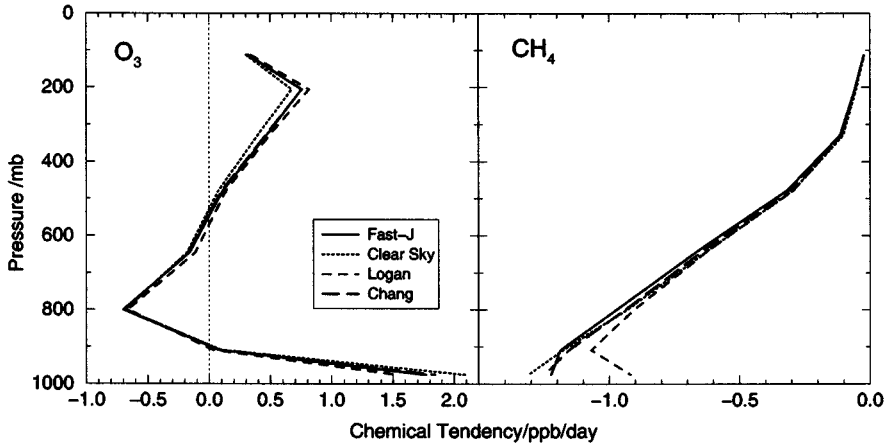

Figure 3. Net chemical tendencies (ppbv/day) of O_3 and CH_4 as a function of pressure (mb). The rates are globally averaged from the UCI CTM for the third week of September and demonstrate the impact of different treatments of photolysis: Clear-sky, Logan and Chang methods, and Fast-J.

The O_3 chemical tendency reflects the more complex couplings between ozone, its precursors, and the photolysis field. Close to the surface, strong ozone formation is seen as the emissions of precursors over continental regions dominate the global mean profile, even though substantial destruction occurs over most of the marine boundary layer. In the mid-troposphere, ozone formation over land is much reduced, and destruction dominates with high levels of water vapour leading to O_3 loss through OH and HO_2 cycles. In the drier upper troposphere, greater efficiency in cycling of NO to NO_2 leads to net ozone production. All the cloud treatments show a reduction in ozone production at the surface and an enhancement in the upper troposphere, but they show a similar degree of ozone destruction in the lower mid-troposphere. Surface ozone production is reduced 15% with Fast-J, 26% with the Logan technique and 12% with the Chang technique; upper tropospheric production is enhanced 15%, 22% and 14%, respectively. Unexpectedly, mid-tropospheric ozone destruction is only affected to a small degree. This region is most influenced by in-cloud photolysis rates and by treatment of multiple cloud layers. It is likely that compensation between competing processes occurs in this region, e.g., Fast-J's greater photolysis of O_3 (leading to loss) is offset by the increase in J_{NO_2} (enhancing NO catalytic formation of O_3). This example highlights the importance of the mid-troposphere in the balance between ozone production and destruction.

The latitude-height structure of the O_3 chemical tendency and the impact of the three cloud treatments are shown for the third week of September in Figure 4. The top-left panel (a) shows the net tendency for clear-sky conditions, revealing largest net O_3 production in the upper tropical troposphere and high production over northern latitude continents extending up to 4 km altitude. The remaining

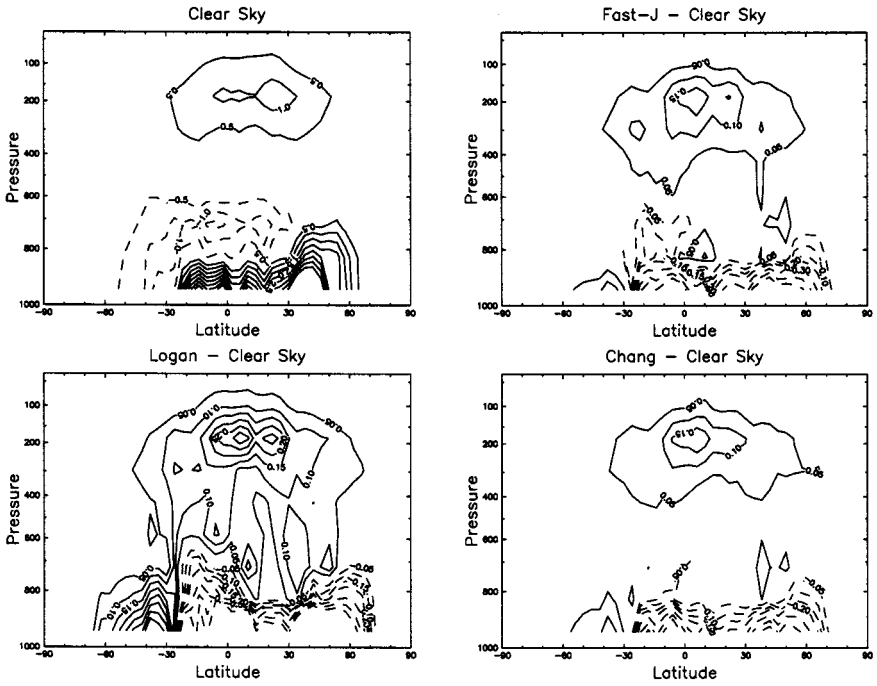

Figure 4. Net chemical tendency of tropospheric O_3 (ppbv/day) as a function of latitude and pressure, integrated zonally for the third week of September from the UCI CTM: (a) shows the O_3 tendency in clear sky conditions, (b) the difference between Fast-J and clear sky, (c) the difference between the Logan method and clear sky, and (d) the difference between the Chang method and clear sky.

panels show the difference in net tendency (with respect to clear sky) of the three cloud treatments: Fast-J in upper-right (b), Logan in lower-left (c), and Chang in lower-right (d). All treatments show less net production in the boundary layer, where reduced photolysis limits ozone formation. They also show more net production in the upper troposphere, where photolysis rates are enhanced. This is the most critical region for ozone as a greenhouse gas and points to the importance of accurate cloud photolysis treatment in chemistry-climate models. The Logan technique exaggerates this effect, and the Chang method does rather poorly in the middle troposphere where the predominant loss of O_3 occurs.

In summary, this sample CTM study with full chemistry demonstrates the importance not only of including cloud cover in photochemical schemes but also of treating it in a thorough and realistic way. This study has minimized the systematic errors in typical parameterizations since zonal averages are compared; though the differences appear small, the strength of Fast-J lies in its representation of known cloud field environments, and hence regional differences may be rather larger. This points to the need for improved quantification of global cloud distribution and cloud properties before significant advances can be made in modelling regional

chemical impacts. Comparison with Fast-J shows that while simple parameterizations may be sufficient under restricted atmospheric circumstances, Fast-J (or an equivalently accurate photolysis scheme) is needed for clouds with a large vertical extent or for commonly-occurring multiple cloud decks and aerosol layers.

5. Conclusions

We present a new code, Fast-J, for calculating photolysis rates in tropospheric models. Like other available methods (e.g., Madronich, 1987; Stamnes *et al.*, 1988; Michelangeli *et al.*, 1992), Fast-J accurately simulates the mean photolytic intensity throughout the atmosphere in the presence of mixed layers of clouds, aerosols, and absorbing gases. Unlike these other methods, however, Fast-J is unique in its design for on-line use in global models with frequent, hourly calls to update photolysis rates. Fast-J solves the full equations of radiative transfer with a reduced expansion of the scattering phase function over a relatively small number of wavelength bins, whilst maintaining the accuracy of the calculated photolysis rates generally to within 3%, and at worst case to about 10%, even in the presence of multiple cloud layers and at high zenith angles. The algorithm used is sufficiently fast to allow incorporation of the scheme in 3-D global CTMs, and hence to allow the full impact of spatially and temporally varying cloud and aerosol layers on tropospheric chemistry to be determined. The scheme may also be used to calculate short-wave heating rates without requiring additional computational resources.

This new scheme is entirely general, uses in real-time the physics predicted in each model layer (e.g., aerosols, clouds, absorbers) and can easily add new photolysis rates at negligible cost. The computation of new photolysis rates is only about a tenth the cost of solving the kinetic equations in the typical cases explored here. Implementing Fast-J in the UCI CTM, we demonstrate the importance of accurate treatment of clouds on the formation of tropospheric ozone. In particular, the different sensitivities of the $J_{O_3/^1D}$ and J_{NO_2} photolysis rates to scattering in and below clouds leads to cloud impacts on net ozone formation rates that are not found in simple parametric models.

The Fast-J code described here is restricted to calculating tropospheric J-values, considering wavelengths down to 289 nm. A stratospheric version, with a greater number of wavelength bins including coverage of shorter wavelengths, is currently under development.

A key limitation of Fast-J and all global chemical models is inability to treat broken cloud fields within a grid box. Even if an improved Fast-J were developed to calculate the photolysis rates between and in clouds, there is no established formalism for treating the inhomogeneous mixture of radical chemistry within a grid.

Copies of the FORTRAN77 program are available from the authors.

Acknowledgements

The authors wish to thank the Interdisciplinary Study Program of the NASA Earth Observing System (EOS/IDS), the NASA Atmospheric Effects of Aviation Program, the NASA Atmospheric Chemistry Modeling and Analysis Program, and the NSF Atmospheric Chemistry Program for their support of this research.

Appendix

A. Scattering in Plane-Parallel Atmospheres with the Anisotropic Feautrier Method

A method of solving for the radiation field in an inhomogeneous, plane-parallel atmosphere with anisotropic scattering is presented. The technique is applicable to stratus-like clouds and aerosol layers but does not address the problem of broken-cloud fields. It is based on the multi-stream method of Feautrier (1964) which has been extended to polarized Rayleigh scattering (Prather, 1974) and to anisotropic scattering by L. H. Auer and M. J. Prather (unpublished, see applications by Cochran and Trafton, 1978; Logan *et al.*, 1981; Jacob *et al.*, 1989). The Feautrier method solves for the specific intensity of the radiation field at a set of zenith angles corresponding to Gauss quadrature points (i.e., discrete ordinates) and at a user-defined set of vertical points in the optical depth coordinate. Its computational advantage lies in the vertical finite-difference formulation that produces a block-tridiagonal system of linear equations with stability and accuracy equivalent to second-order, finite-difference solutions. Further, the numerical solution is only linearly proportional to the number of vertical levels. The notation and equations below are based on the integro-differential form of Chandrasekhar (1960). The basic definitions are given in Table I, and the generic equations for the monochromatic scattering problem in Table II.

Following Chandrasekhar (1960) the basic equation of radiative transfer for a scattering atmosphere with an incoming solar beam (Equation (1)) is solved by expanding the scattering phase function into Legendre (Equation (2)) and Associated Legendre functions (Equation (3); Dave and Armstrong, 1970). The specific intensity is likewise expanded in a Fourier series about the cosine of the azimuth angle (Equation (4)), and each moment of the intensity is solved for separately (Equations (5) and (6)). The mean specific intensity is only a function of the zeroth component of this Fourier series (Equation (7)), and the photolytic intensity J (proportional to the photolysis rate) is then the sum of the solar flux (perpendicular to the beam) plus the 4π-integrated specific intensity (Equation (8)).

The unique approach here, shown in Table III, is to separate the specific intensity into symmetric (j) and asymmetric (h) terms (Equation (9)). Using the symmetry properties of the Legendre functions (Equations (10) and (11)), we are able to decompose the original integro-differential equation (Equation (1)) into

Table I. Definitions of radiative transfer quantities

τ = optical depth (dimensionless)
μ = consine of zenith angle (dimensionless)
μ_0 = cosine of solar zenith angle (dimensionless)
ϕ = azimuth angle (radians)
ϕ_0 = solar azimuth angle (radians)
πF = top-of-atmosphere solar flux (photons cm^{-2} s^{-1})
parallel beam directed along $(-\mu_0, \phi_0)$
$l(\tau, \mu, \phi)$ = specific intensity (photons cm^{-2} s^{-1} ster^{-1})
looking in direction (μ, ϕ) at optical depth level τ
$J(\tau)$ = mean intensity (photons cm^{-2} s^{-1}) used for photolysis rates
$p(\tau, \cos\Theta)$ = scattering phase function (ster^{-1})
probability of scatter by angle Θ at optical depth level τ
$\cos\Theta \equiv \mu\mu' + (1-\mu^2)^{1/2}(1-\mu'^2)^{1/2}\cos(\phi-\phi')$
$p(\tau, \mu, \phi, \mu', \phi')$ = probability of scattering (ster^{-1}) from
direction (μ', ϕ') into direction (μ, ϕ) at optical depth level τ
$\omega^k(\tau)$ = kth Legendre coefficient of expansion of $P(\tau, \cos\Theta)$ (dimensionless, $\omega^0 \equiv 1$)
$\overline{\omega}(\tau)$ = single scattering albedo (dimensionless) at optical depth level τ
= ratio of scattering to scattering plus absorption
$P_k(\mu)$ = kth Legendre polynomial of $\mu(-1 \leqslant \mu \leqslant +1)$ (dimensionless)
$Y_k^m(\mu)$ = Associated Legendre function ($Y_k^0 \equiv P_k$)
$Y_k^m(-\mu) = (-1)^{k-m} Y_k^m(\mu)$

a pair of coupled first-order integro-differential equations: The first derivative of the symmetric j's is only a function of the h's (Equation (12a)), and that of the asymmetric h's is only a function of the symmetric j's (Equation (12b)). Note also that the Fourier expansion in azimuth similarly separates (Equation (13)). In order to solve for the specific intensity of skylight in any direction, the complete set of azimuthal expansions must be solved. Since this paper focuses on the photolytic intensity (Equation (14)), we continue the description of the solution using only the zeroth azimuthal expansion, although the approach can be applied to all orders of the expansion.

For the case of isotropic or Rayleigh scattering the odd terms in Equations (12a) and (13a) vanish, and the coupled pair of equations can be readily collapsed into a single second-order differential equation involving only the symmetric j's. This second-order ordinary differential equation can be solved accurately and efficiently by finite-difference approximation over the optical depth grid with second-order boundary conditions (Auer, 1967). For Rayleigh scattering ($K = 2$), the azimuth Fourier expansion extends only to $m = 0, 1, 2$ (Prather, 1974).

Table II. Fourier decomposition of the equation of radiative transfer (Chandrasekhar, 1960)

$$\mu \frac{dI(\tau,\mu,\phi)}{d\tau} = l(\tau,\mu,\phi) - \frac{\overline{\omega}(\tau)}{4\pi}\int_{-1}^{+1} d\mu' \int_0^{2\pi} d\phi' p(\tau,\mu,\phi,\mu',\phi') l(\tau,\mu',\phi') - \\ - \frac{\overline{\omega}(\tau)}{4} p(\tau,\mu,\phi,-\mu_0,\phi_0) F e^{-\tau/\mu_0} \quad (1)$$

$$p(\tau,\cos\Theta) = \sum_{k=0}^{K} \omega^k(\tau) P_k(\cos\Theta) \quad (2)$$

$$p(\tau,\mu,\phi,\mu',\phi') = \sum_{k=0}^{K} \omega^k(\tau) P_k(\mu) P_k(\mu') + \\ + 2\sum_{m=1}^{K}\sum_{k=m}^{K} \omega^k(\tau) Y_k^m(\mu) Y_k^m(\mu') \cos(m(\phi-\phi')) \quad (3)$$

$$I(\tau,\mu,\phi) = \sum_{m=0}^{K} I^m(\tau,\mu)\cos(m(\phi-\phi_0)) \quad (4)$$

$$\mu \frac{dI^0(\tau,\mu)}{d\tau} = I^0(\tau,\mu) - \frac{\overline{\omega}(\tau)}{2}\sum_{k=0}^{K} \omega^k(\tau) P_k(\mu) \int_{-1}^{+1} d\mu' P_k(\mu') I^0(\tau,\mu') - \\ - \frac{\overline{\omega}(\tau)}{4} F\, e^{-\tau/\mu_0} \sum_{k=0}^{K} \omega^k(\tau) P_k(\mu) P_k(-\mu_0) \quad (5)$$

$$\mu \frac{dI^m(\tau,\mu)}{d\tau} = I^m(\tau,\mu) - \frac{\overline{\omega}(\tau)}{2}\sum_{k=0}^{K} \omega^k(\tau) Y_k^m(\mu) \int_{-1}^{+1} d\mu' Y_k^m(\mu') I^m(\tau,\mu') - \\ - \frac{\overline{\omega}(\tau)}{2} F\, e^{-\tau/\mu_0} \sum_{k=0}^{K} \omega^k(\tau) Y_k^m(\mu) Y_k^m(-\mu_0) \quad (6)$$

$$\langle I(\tau)\rangle = \frac{1}{4\pi}\int_{-1}^{+1} d\mu \int_0^{2\pi} d\phi I(\tau,\mu,\phi) = \frac{1}{2}\int_{-1}^{+1} d\mu I^0(\tau,\mu) \quad (7)$$

$$J(\tau) = \pi F_0 e^{-\tau/\mu_0} + 4\pi \langle I(\tau)\rangle \quad (8)$$

The integro-differential equations for j and h are solved at a set of discrete optical depths and zenith angles as per Feautrier (1964) with notation given in Table IV. The set of coupled first-order equations easily lend themselves to a leapfrog-like set of finite difference equations outlined in Table V. The asymmetric scattering terms involving h's are only defined at the intermediate even-numbered points (Equation (16)), and thus their first derivative is defined at the odd points (Equation (17)). In parallel, the symmetric j's are defined at the upper (Equation

Table III. Solution of the equation of radiative transfer with Odd-Even Functions

$$j^m(\tau,\mu) \equiv \frac{1}{2}[I^m(\tau,+\mu) + I^m(\tau,-\mu)], \quad 0 \leqslant \mu \leqslant 1 \tag{9a}$$

$$h^m(\tau,\mu) \equiv \frac{1}{2}[I^m(\tau,+\mu) - I^m(\tau,-\mu)], \quad 0 \leqslant \mu \leqslant 1 \tag{9b}$$

$$\begin{aligned}\int_{-1}^{+1} d\mu P_k(\mu) I^0(\tau,\mu) &= 2\int_0^{+1} d\mu P_k(\mu) j^0(\tau,\mu) \text{ for } k \text{ even} \\ &= 2\int_0^{+1} d\mu P_k(\mu) h^0(\tau,\mu) \text{ for } k \text{ odd}\end{aligned} \tag{10}$$

$$\begin{aligned}\int_{-1}^{+1} d\mu Y_k^m(\mu) I^m(\tau,\mu) &= 2\int_0^{+1} d\mu Y_k^m(\mu) j^m(\tau,\mu) \text{ for } k-m \text{ even} \\ &= 2\int_0^{+1} d\mu Y_k^m(\mu) h^m(\tau,\mu) \text{ for } k-m \text{ odd}\end{aligned} \tag{11}$$

$$\begin{aligned}\mu\frac{dj^0(\tau,\mu)}{d\tau} &= h^0(\tau,\mu) - \overline{\omega}(\tau)\sum_{\text{odd } k}\omega^k(\tau)P_k(\mu)\int_0^{+1} d\mu' P_k(\mu') h^0(\tau,\mu') - \\ &\quad - \frac{\overline{\omega}(\tau)}{4} F\, e^{-\tau/\mu_0}\sum_{\text{odd } k}\omega^k(\tau)P_k(\mu)P_k(-\mu_0)\end{aligned} \tag{12a}$$

$$\begin{aligned}\mu\frac{dh^0(\tau,\mu)}{d\tau} &= j^0(\tau,\mu) - \overline{\omega}(\tau)\sum_{\text{even } k}\omega^k(\tau)P_k(\mu)\int_0^{+1} d\mu' P_k(\mu') j^0(\tau,\mu') - \\ &\quad - \frac{\overline{\omega}(\tau)}{4} F\, e^{-\tau/\mu_0}\sum_{\text{even } k}\omega^k(\tau)P_k(\mu)P_k(-\mu_0)\end{aligned} \tag{12b}$$

$$\begin{aligned}\mu\frac{dj^m(\tau,\mu)}{d\tau} &= h^m(\tau,\mu) - \overline{\omega}(\tau)\sum_{\text{odd } k-m}\omega^k(\tau)Y_k^m(\mu)\int_0^{+1} d\mu' Y_k^m(\mu') h^m(\tau,\mu') - \\ &\quad - \frac{\overline{\omega}(\tau)}{2} F\, e^{-\tau/\mu_0}\sum_{\text{odd } k-m}\omega^k(\tau)Y_k^m(\mu)Y_k^m(-\mu_0)\end{aligned} \tag{13a}$$

$$\begin{aligned}\mu\frac{dh^m(\tau,\mu)}{d\tau} &= j^m(\tau,\mu) - \overline{\omega}(\tau)\sum_{\text{even } k-m}\omega^k(\tau)Y_k^m(\mu)\int_0^{+1} d\mu' Y_k^m(\mu') j^m(\tau,\mu') - \\ &\quad - \frac{\overline{\omega}(\tau)}{2} F\, e^{-\tau/\mu_0}\sum_{\text{even } k-m}\omega^k(\tau)Y_k^m(\mu)Y_k^m(-\mu_0)\end{aligned} \tag{13b}$$

$$J(\tau) = \pi F_0 e^{-\tau/\mu_0} + 4\pi\int_0^{+1} d\mu j^0(\tau,\mu) \tag{14}$$

Table IV. Grid points in optical depth and angle quadrature

$\{\mu_n, a_n\}$ = Gauss points and weights over interval: [0, 1], $n = 1, N$

$$\Longrightarrow \int_0^{+1} d\mu F(\mu) = \sum_{n=1}^{N} F(\mu_n) a_n$$

Legendre expansion: $k = 0, K$ ($\leqslant 2N - 1$)

$\{\tau_i\}$ = Optical depth grid over interval $i = 1, L$

$\tau_1 = 0$ = top-of-atmosphere

$\tau_L = \mathrm{T}$ = surface

λ = albedo of Lambert surface at $\tau_L = \mathrm{T}$

$j_{in} \equiv j^0(\tau_i, \mu_n)$ defined for odd $i = 1, 3, 5, \ldots, L$

$h_{in} \equiv h^0(\tau_i, \mu_n)$ defined for even $i = 2, 4, 6, \ldots, L - 1$

$P_k^n \equiv P_k(\mu_n)$

$\overline{\omega}_i \equiv \overline{\omega}(\tau_i)$

$\omega_i^k \equiv \omega^k(\tau_i)$

$F_i \equiv F\, e^{-\tau_i/\mu_0}$

$$J(\tau_i) = J_i = \pi F_i + 4\pi \sum_{n=1}^{N} j_{in} a_n \qquad (15)$$

(18)), lower (Equation (19)), and all odd-numbered points in between (Equation (17)), and their derivative is defined at even-numbered points. This set of equations reduces to a block-tridiagonal system; the diagonal block is in general full, comprising the appropriately weighted scattering matrix (right-hand side of Equation (16) and (17)), and the off-diagonal blocks are diagonal (left-hand side of Equations (16) and (17)). The upper and lower boundaries are derived from a Taylor series expansion about the endpoints, using the first-derivative evaluated at the endpoint, per Equation (12b). At the lower boundary we adopt a Lambertian surface that isotropically reflects a fraction (λ) of the incident flux. These boundary conditions complete the block tridiagonal system that can be solved (Feautrier, 1964) for the symmetric j's and hence photolytic intensity J (Eq. 15) at all the odd points. The net flux crossing each level can be calculated from the asymmetric h's at each intermediate even point, and hence the flux divergence or heating rate is available with the j's at the odd points.

This $LN \times LN$ system of linear equations is efficiently solved as a block tridiagonal system of equations with $N \times N$ blocks (Feautrier, 1964). Results from the forward pass through the system can be saved and used to recompute the solution for a different right-hand side (i.e., different solar zenith angles) at negligible computational cost. The right-hand side involves only terms proportional to $F(\tau)$,

Table V. Finite-difference equations for block-tridiagonal system (Feautrier, 1964)

at intermediate EVEN points ($i = 2, 4, 6, \ldots, L-1$)

$$\mu_n(j_{i+1,n} - j_{i-1,n})/(\tau_{i+1} - \tau_{i-1}) =$$

$$h_{in} - \overline{\omega}_i \sum_{k=1,3,\ldots}^{2N-1} \omega_i^k P_k^n \sum_{m=1}^{N} P_k^m h_{im} a_m - \frac{\overline{\omega}_i F_i}{4} \sum_{k=1,3,\ldots}^{2N-1} \omega_i^k P_k^n P_k(-\mu_0) \tag{16}$$

at intermediate ODD points ($i = 3, 5, \ldots, L-2$)

$$\mu_n(h_{i+1,n} - h_{i-1,n})/(\tau_{i+1} - \tau_{i-1}) =$$

$$j_{in} - \overline{\omega}_i \sum_{k=0,2,\ldots}^{2N-2} \omega_i^k P_k^n \sum_{m=1}^{N} P_k^m j_{im} a_m - \frac{\overline{\omega}_i F_i}{4} \sum_{k=0,2,\ldots}^{2N-2} \omega_i^k P_k^n P_k(-\mu_0) \tag{17}$$

at the UPPER boundary ($i = 1$): $h_{2,n} = h_{1,n} + (\tau_2 - \tau_1)\left.\frac{\partial h_n}{\partial \tau}\right|_1 +$ 2nd-order terms

use $I(0, -\mu_n) = 0 \Rightarrow h_{1,n} = j_{1,n} \Rightarrow$

$$h_{2,n} = j_{1,n} + \frac{(\tau_2 - \tau_1)}{\mu_n} \times$$

$$\times \left[j_{1,n} - \overline{\omega}_1 \sum_{k=0,2,\ldots}^{2N-2} \omega_1^k P_k^n \sum_{m=1}^{N} P_k^m j_{1,m} a_m - \frac{\overline{\omega}_1 F_1}{4} \sum_{k=0,2,\ldots}^{2N-2} \omega_1^k P_k^n P_k(-\mu_0) \right] \tag{18}$$

at the LOWER boundary ($i = L$): $h_{L-1,n} = h_{L,n} - (\tau_L - \tau_{L-1})\left.\frac{\partial h_n}{\partial \tau}\right|_L +$ 2nd-order terms

use Lambertian surface (λ): $I^0(\tau_L, +\mu_n) = I_L^+ = \frac{4\lambda}{1+\lambda} \sum_{m=1}^{N} j_{L,m} \mu_m a_m$

$\Rightarrow h_{L,n} = I_L^+ - j_{L,n} \Rightarrow$

$$h_{L-1,n} = I_L^+ - j_{L,n} - \frac{(\tau_L - \tau_{L-1})}{\mu_n} \times$$

$$\times \left[j_{L,n} - \overline{\omega}_L \sum_{k=0,2,\ldots}^{2N-2} \omega_L^k P_k^n \sum_{m=1}^{N} P_k^m j_{L,m} a_m - \frac{\overline{\omega}_L F_L}{4} \sum_{k=0,2,\ldots}^{2N-2} \omega_L^k P_k^n P_k(-\mu_0) \right] \tag{19}$$

and the entire solution is, of course, linear in F. An obvious consequence of this linearity is that the average scattered intensity over a day can be derived with a single calculation by first averaging the source term, the last term in Equation (5).

B. Approximating the Scattering Phase Function

The multiple scattering problem in a plane-parallel geometry can be solved to any accuracy for scattering phase functions that depend only on the scattering angle, as shown in Appendix A. The major computational difficulty with such solutions lies in the accurate expansion of the scattering phase function with Legendre polyno-

mials (Table II, Equation (2)) and hence in the number of Gauss points needed to represent and integrate over the high-order polynomials (Table IV). For example, Rayleigh-phase scattering (without polarization) has an easy, finite expansion stopping at $K = 2$: $p^{R\text{-phase}} = 1 \times P_0 + 1/2 \times P_2$. In this case, the use of $N = 3$ (Gauss points over the interval 0 to 1) more than adequately resolves the scattered field and yields an easy-to-solve tridiagonal matrix with internal blocks of size 3×3. For larger particles typical of atmospheric aerosols and clouds, the scattering phase function is strongly peaked in the forward direction, becoming more so as the particles become larger. Resolution of this forward scattering peak for μm-size particles can require Legendre expansions out to $K = 100$ or more, requiring $N = 50$ or larger. The numerical cost of the Feautrier solution is proportional to N^3.

A sample of the scattering phase function at 400 nm for water clouds with different droplet size distributions is shown in Figure 5. The Deirmendjian (1969) cloud types cumulus-1 (C1) and haze-1 (H1) have been adopted; these are pure Gamma distributions (see also Hansen and Travis, 1974) and are described in Table VI. The scattering phase function for these homogeneous water droplets is calculated with the Mie code of Hansen and Travis (1974; A. Lacis, personal communication, 1988). Clouds with larger mode radii have more strongly forward peaked distributions. For example, the haze function with mode radius of 0.1 μm (H1(0.1)) has a forward-peak value of about 24, whereas the cumulus function with mode radius of 13.3 μm (C1(13)) has a forward-peak value greater than 30000. The phase functions for C1(2) and C1(4) are also shown.

The expansion coefficients, ω^k, of these four phase functions are shown in Figure 6. For strongly forward-peaked phase functions these coefficients increase initially as $2k + 1$ and then decrease to zero as the phase function is resolved. The H1(0.1 μm) is well represented by an expansion to $K = 16$, whereas that of C1(2 μm) requires about $K = 160$, and the coefficients of C1(13 μm) are still increasing at $K = 160$. The effective scattering phase function for two truncated expansions of C1(2) are shown in Figure 7. The thin black line ($K = 160$) describes the exact phase function very well over more than four orders of magnitude, but the truncation at $K = 8$ produces a non-physical phase function with negative lobes. The scattering phase function is not a strong function of wavelength over the region of interest (300–800 nm) as shown for the C1(4) distribution in Figure 8.

The C1(2) water cloud can be solved practically with high numerical accuracy using the $K = 160$ expansion of the phase function. Using a finite-difference grid in optical depth (τ) of $L = 101$, the matrix form (see Table V) has an overall size of 8080 $\times$ 8080, which would be beyond the practical limit were it not for the Feautrier block-tridiagonal structure (the internal matrix blocks are only 80 $\times$ 80). An 'exact' calculation ($K/N = 160/80$) of the monochromatic photolytic intensity J is made for several cases. In Figure 9 the value J is shown throughout a cloud of optical depth 20 above a Lambertian surface with reflectivity of 0.10 for both overhead sun ($\mu_o = 1.0$, left) and $\mu_o = 0.5$ (right). The calculation

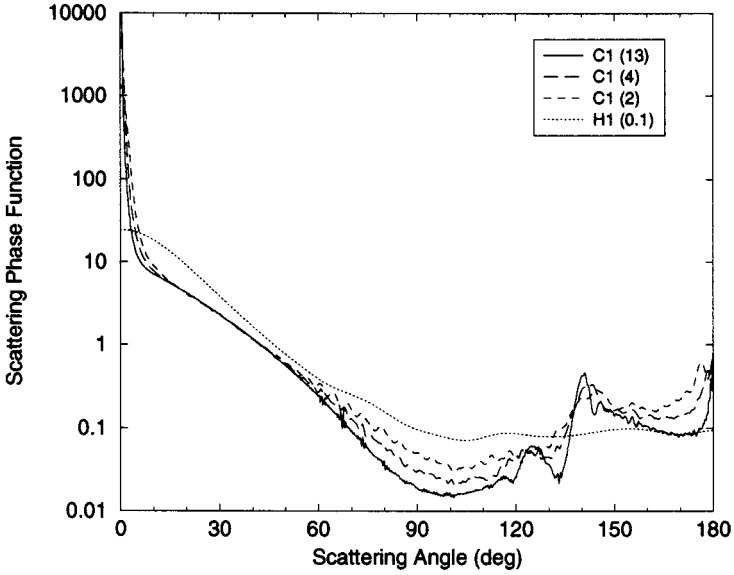

Figure 5. Scattering phase function at 400 nm for water clouds with Deirmendjian (1969) distributions for cumulus clouds-1 (C1 (13.3 μm mode radius), solid line; C1 (4 μm), long-dashed; C1 (2 μm), dashed) and haze-1 (H1 (0.1 μm), dotted). This sequence is in descending order at the forward peak (0°) and ascending order at the minimum phase function (100°).

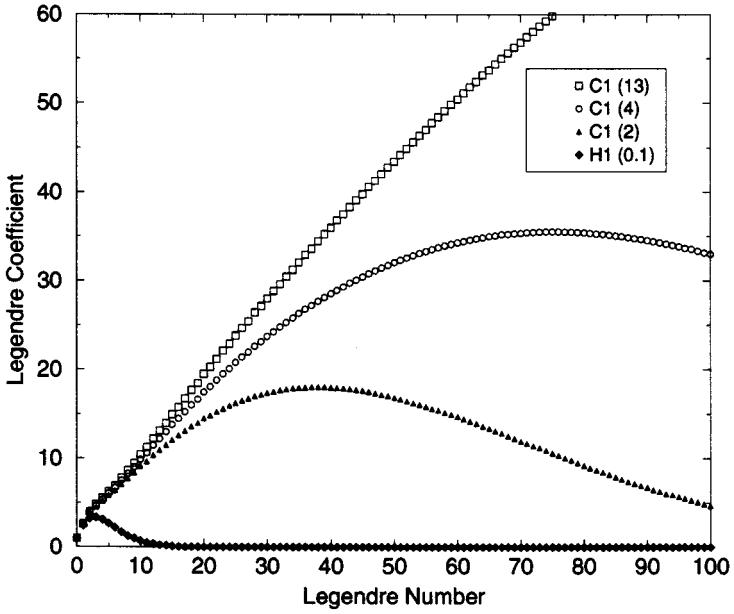

Figure 6. Legendre coefficients for the expansion of the scattering phase functions in Figure 5: C1 (13.3 μm mode radius), open squares; C1 (4 μm), open circles; C1 (2 μm), solid triangles; H1 (0.1 μm), solid diamonds.

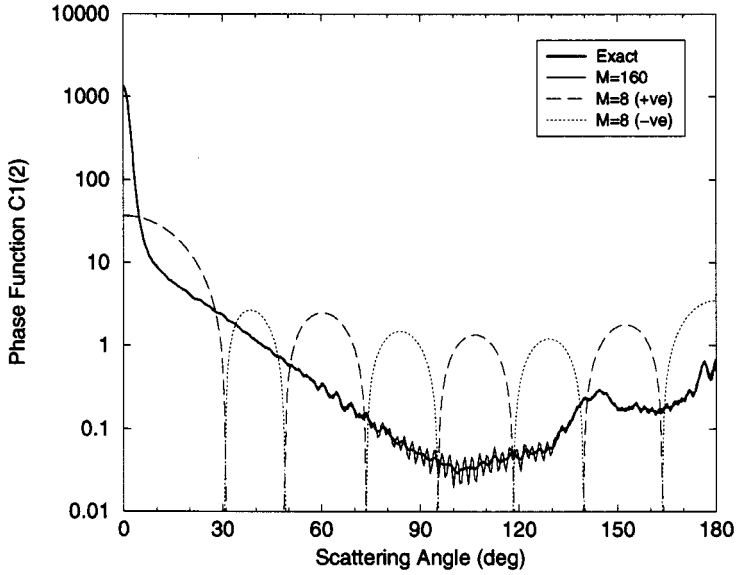

Figure 7. Scattering phase function for C1 (2 μm mode radius) for 400 nm for different truncations. The exact phase function is given by the thick line; that represented by a 160-term expansion, by the thin (more jagged) line; and that from the 8-term expansion, by the dashed and dotted lines. The 8-term expansion has negative values for the phase function that are shown on this logarithmic scale with dotted lines.

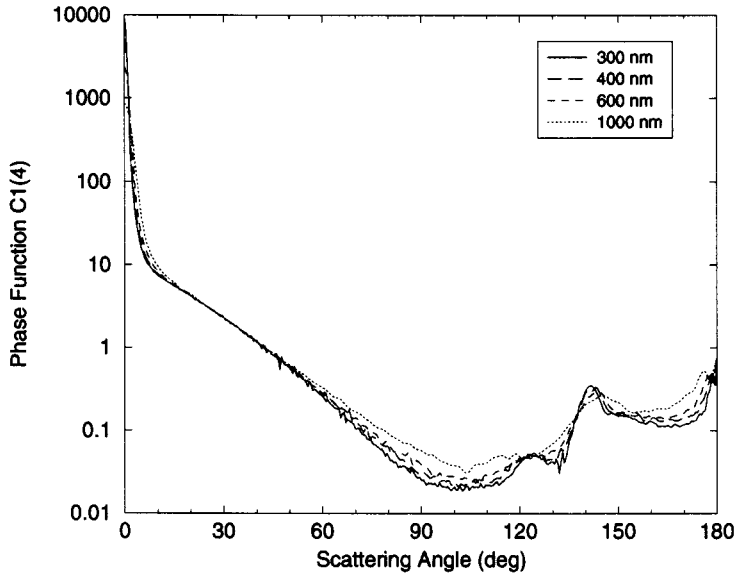

Figure 8. Scattering phase function for water cloud C1 (4 μm mode radius) for different wavelengths. The scattering is most strongly forward peaked for shorter wavelengths, but shows only small differences in the range 300–600 nm.

Table VI. Cloud and aerosol droplet distributions

Water Clouds (index of refraction = 1.335 + 0i):
Gamma Distribution (droplet radius = r):

$n(r) = ar^{\alpha}e^{-br}$ has a maximum at $r_{\text{mode}} = \alpha/b$ [μm or cm]

$$N = \int_0^{\infty} n(r)dr = ab^{-(\alpha+1)}\Gamma(\alpha+1) \text{ [particles cm}^{-3}\text{]}$$

$$G = \int_0^{\infty} \pi r^2 n(r)dr \text{ [cm}^2 \text{ cm}^{-3}\text{]}$$

$$r_{eff} = \int_0^{\infty} r\,\pi r^2 n(r)dr/G \text{ [cm]}$$

$$V = \int_0^{\infty} \tfrac{4}{3}\pi r^3 n(r)dr = \tfrac{4}{3}G\,r_{eff} \text{ [cm}^3 \text{ cm}^{-3}\text{]}$$

Mie theory gives the extinction efficiency Q for this distribution:

$$Q_{ext} = Q_{scat} + Q_{abs} = Q_{scat} = \frac{1}{G}\frac{d\tau}{dz}$$

Water column density:

$\frac{4}{3}r_{eff}\tau/Q_{ext}$ [10^{-3} kg m^{-2}] where r_{eff} is in μm.

Deirmendjian cumulus type C1: $\alpha = 6$, $r_{eff} = \frac{3}{2}r_{\text{mode}}$
Deirmendjian haze type H1: $\alpha = 2$, $r_{eff} = \frac{5}{2}r_{\text{mode}}$

Stratospheric Sulfate Layer (index of ref. = 1.46 + 0i):
Log-normal Distribution (droplet radius = r):

$$n(r) = \frac{1}{\sqrt{2\pi}\sigma}\frac{1}{r}\exp\left[\frac{-(\ln r - \ln r_g)^2}{2\sigma^2}\right]$$

background layer: $r_g = 0.09$ μm, $\sigma = 0.6$
volcanically perturbed: $r_g = 0.08$ μm, $\sigma = 0.8$

was repeated with a drastically truncated phase function: $K/N = 8/4, 6/3$, and $4/2$. Surprisingly the $K/N = 8/4$ preserves most of the accuracy of the near exact solution at a substantially lower computational cost. The relative error of the $K/N = 8/4$ solution is generally less than 5% over the full range of optical depths and zenith angles shown, whereas the more severely truncated forms with $K/N = 6/3$ and $K/N = 4/2$ have substantially larger errors, usually near the top of the cloud. Results for a thinner cloud of optical depth 4 are shown in Figure 10. The error with $K/N = 8/4$ is slightly larger, but is still only a maximum of 8% near the top of the cloud. Approximating the scattered field with only 2 or 3 angles, however, yields errors that are two to four times greater.

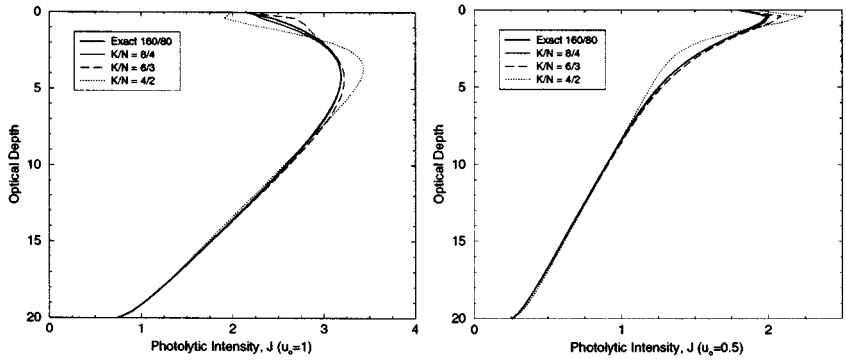

Figure 9. Photolytic intensity J throughout a cloud of optical depth 20 for different approximations of the scattering phase function (labeled K/N where K is the order of the Legendre expansion (see Figure 6), and N is the number of Gauss points). The top of the water cloud (C1 (2 μm) at 400 nm) is at optical depth 0, and the cloud lies over a Lambertian surface of albedo 0.1. The finite difference equations in optical depth were solved at 101 levels and the exact solution is calculated with $K/N = 160/80$. (Left) With overhead sun ($\mu_o = 1.0$) of intensity $F = 1.0$. The maximum relative error for $K/N = 8/4$, 6/3, and 4/2 is 5% (barely visible), 10%, and 22% respectively. (Right) With solar zenith angle 60° ($\mu_o = 0.5$). The maximum relative error for $K/N = 8/4$, 6/3, and 4/2 is 1% (not visible), 5%, and 12% respectively.

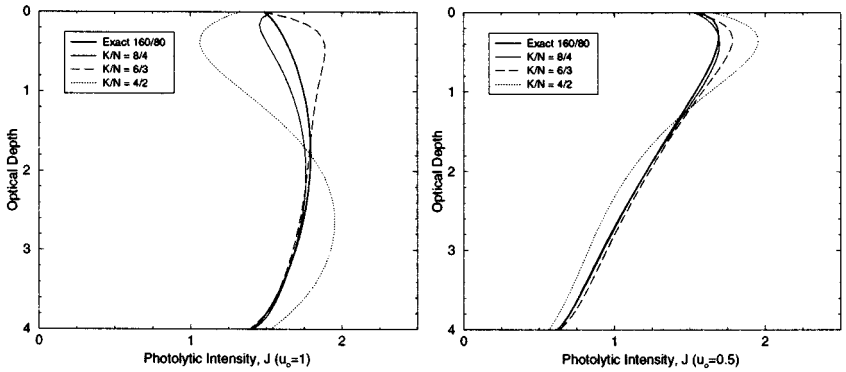

Figure 10. Photolytic intensity J throughout a cloud of optical depth 4 for different approximations of the scattering phase function (labeled K/N), see Figure 9. The top of the water cloud (C1 (2μm) at 400 nm) is at optical depth 0, and the cloud lies over a Lambertian surface of albedo 0.1. (Left) With overhead sun ($\mu_o = 1.0$) of intensity $F = 1.0$. The maximum relative error for $K/N = 8/4$, 6/3, and 4/2 is 8%, 16%, and 35% respectively. (Right) With solar zenith angle 60° ($\mu_o = 0.5$). The maximum relative error for $K/N = 8/4$, 6/3, and 4/2 is 2% (barely visible), 6%, and 16% respectively.

What is lost in this approximation of $K/N = 8/4$? The radiative transfer equation is being solved for with a phase function that includes negative lobes, and the resulting solution will not produce meaningful specific intensities ($I(\tau, \mu, \phi)$), yet the mean photolytic value J is computed accurately. One key advantage of this approach is that the exact phase function can be directly put into the numerical

solution. For many other approaches that rely on resolving the phase function (e.g., without negative lobes) it is often required that the actual phase function be approximated as isotropic plus forward peak, or as only the first term in the expansion ($g = \overline{\cos} = \omega^1/3$). Given the fast Feautrier method, there is little computational advantage to reducing the angular resolution below $K/N = 8/4$, and the errors grow substantially as one goes to a two-stream (i.e., 1 angle) approximation.

A sample of aerosol and cloud phase functions for use in Fast-J are given in Table VII. The sulfate and water aerosol scattering properties were calculated with the Mie code from A.A. Lacis and the ice phase functions were supplied by M. Mishchenko. For the two cases of stratospheric sulfate aerosols, the size distributions are fitted to the pre- and post-Pinatubo observations (Wilson *et al.*, 1993; Brock *et al.*, 1993). The sizes of these particles are comparable to the range of visible wavelengths and hence both extinction efficiency Q and phase function ω^k vary with wavelength. The water haze (H1) with mode radius of 0.1 μm has similar properties. For water clouds (C1 and L) with mode radii greater than 2 μm, however, there are only small changes of optical properties across the visible wavelengths, i.e., these clouds are effectively 'white'. The ice optical properties correspond to two widely accepted shape models for cirrus crystals: hexagonal particles and highly irregular particles (Mishchenko *et al.*, 1996). The shape variability is much stronger than the size variability, especially for the asymmetry parameter of the phase function (i.e., $\omega^1/3$). These two models represent limiting cases for ice crystal properties. The ice-irregular model is implemented in the ISCCP ice retrieval algorithm. The inclusion of optical properties for 999 nm in these sample phase functions is given primarily as a convenience since the optical depth of aerosol/cloud layers may be reported at a wavelength of 1 μm.

How important is the choice of the phase function? The relative photolytic intensity J at 400 nm is calculated for a standard atmosphere with Rayleigh-phase scattering and an embedded cloud of optical depth 20 placed uniformly between 1 and 17 km. A lower surface Lambertian albedo of 0.10 is adopted. The primary solar term is calculated with a spherical atmosphere but without refraction (Logan *et al.*, 1981). Results for 5 different scattering phase functions are shown in Figure 11 (top panels). For overhead sun ($\mu_o = 1$) the value of J peaks between 10 and 16 km altitude at more than 3 times the top-of-atmosphere direct solar value, and falls to less than 1 times this value at the surface. For lower sun ($\mu_o = 0.5$) the peak J, about 2, is located narrowly at about 16 km altitude, and the surface value is less than 0.3. The choice of phase function is clearly important for $\mu_o = 1$. The two phase functions for large water drops (C1 with mode radii of 4 and 13 μm) are distinguishable but very close and best represent a typical cumulus liquid water cloud. The use of isotropic scattering is grossly in error as expected, and the use of a haze with small particles (0.1 μm) lies in between. Large hexagonal ice crystals produce more large-angle scattering like the H1 (0.1 μm) distribution. For lower sun ($\mu_o = 0.5$), the isotropic and haze phase functions are clearly in error, but any of the 'large-particle' phase functions are indistinguishable. For deep liquid water

Table VII. Scattering properties for different media for Fast-J

λ (nm)	Q	r_{eff}	$\bar{\omega}_o$	ω^0	ω^1	ω^2	ω^3	ω^4	ω^5	ω^6	ω^7
Rayleigh											
300	123.5	0.001	1.000	1.000	0.0	0.500	0.0	0.0	0.0	0.0	0.0
400	39.1	0.001	1.000	1.000	0.0	0.500	0.0	0.0	0.0	0.0	0.0
600	7.7	0.001	1.000	1.000	0.0	0.500	0.0	0.0	0.0	0.0	0.0
999	1.0	0.001	1.000	1.000	0.0	0.500	0.0	0.0	0.0	0.0	0.0
Isotropic											
300	1.0	0.001	1.000	1.000	0.0	0.0	0.0	0.0	0.0	0.0	0.0
400	1.0	0.001	1.000	1.000	0.0	0.0	0.0	0.0	0.0	0.0	0.0
600	1.0	0.001	1.000	1.000	0.0	0.0	0.0	0.0	0.0	0.0	0.0
999	1.0	0.001	1.000	1.000	0.0	0.0	0.0	0.0	0.0	0.0	0.0
Fully absorbing 'soot'											
300	1.0	0.001	0.000	1.000	0.0	0.0	0.0	0.0	0.0	0.0	0.0
400	1.0	0.001	0.000	1.000	0.0	0.0	0.0	0.0	0.0	0.0	0.0
600	1.0	0.001	0.000	1.000	0.0	0.0	0.0	0.0	0.0	0.0	0.0
999	1.0	0.001	0.000	1.000	0.0	0.0	0.0	0.0	0.0	0.0	0.0
Stratospheric sulfate, background											
300	2.7541	0.221	1.000	1.000	2.157	2.767	2.627	2.457	2.098	1.792	1.518
400	2.4017	0.221	1.000	1.000	2.146	2.641	2.422	2.122	1.709	1.357	1.070
600	1.6454	0.221	1.000	1.000	2.076	2.377	2.023	1.608	1.177	0.846	0.599
999	0.7449	0.221	1.000	1.000	1.877	1.920	1.412	0.970	0.614	0.388	0.238
Stratospheric sulfate, volcanic											
300	2.6437	0.386	1.000	1.000	2.152	2.901	2.856	2.971	2.772	2.709	2.587
400	2.5603	0.386	1.000	1.000	2.142	2.810	2.706	2.691	2.421	2.254	2.066
600	2.2221	0.386	1.000	1.000	2.127	2.673	2.488	2.308	1.963	1.698	1.461
999	1.5319	0.386	1.000	1.000	2.076	2.458	2.165	1.841	1.449	1.142	0.898
Water haze H1 (0.1 μm)											
300	2.8438	0.25	1.000	1.000	2.454	3.376	3.624	3.608	3.300	2.911	2.526
400	2.3497	0.25	1.000	1.000	2.431	3.235	3.355	3.108	2.686	2.180	1.690
600	1.4037	0.25	1.000	1.000	2.328	2.789	2.593	2.062	1.492	1.013	0.632
999	0.5034	0.25	1.000	1.000	1.916	1.870	1.233	0.704	0.338	0.154	0.062
Water haze H1 (0.4 μm)											
300	2.2995	1.00	1.000	1.000	2.433	3.625	4.104	4.645	5.020	5.409	5.802
400	2.4743	1.00	1.000	1.000	2.341	3.475	3.863	4.330	4.589	4.878	5.125
600	2.6719	1.00	1.000	1.000	2.325	3.334	3.624	3.896	3.939	3.968	3.964
999	2.9565	1.00	1.000	1.000	2.434	3.393	3.685	3.709	3.528	3.213	2.903
Water cloud C1 (2.0 μm)											
300	2.1410	3.00	1.000	1.000	2.544	3.886	4.572	5.256	5.933	6.530	7.291
400	2.1778	3.00	1.000	1.000	2.513	3.834	4.480	5.160	5.785	6.356	7.044
600	2.2287	3.00	1.000	1.000	2.483	3.767	4.359	4.998	5.542	6.054	6.639
999	2.3071	3.00	1.000	1.000	2.395	3.597	4.063	4.648	5.052	5.478	5.857

Table VII. (Continued)

λ (nm)	Q	r_{eff}	$\bar{\omega}_o$	ω^0	ω^1	ω^2	ω^3	ω^4	ω^5	ω^6	ω^7
Water cloud C1 (4.0 μm)											
300	2.0835	6.00	1.000	1.000	2.596	3.973	4.725	5.406	6.129	6.751	7.607
400	2.1064	6.00	1.000	1.000	2.571	3.936	4.660	5.345	6.056	6.670	7.492
600	2.1345	6.00	1.000	1.000	2.557	3.902	4.596	5.263	5.923	6.507	7.267
999	2.1922	6.00	1.000	1.000	2.499	3.799	4.418	5.081	5.667	6.213	6.851
Water cloud C1 (8.0 μm)											
300	2.0539	12.00	1.000	1.000	2.619	4.013	4.798	5.476	6.232	6.870	7.780
400	2.0643	12.00	1.000	1.000	2.611	3.999	4.773	5.451	6.194	6.826	7.716
600	2.0883	12.00	1.000	1.000	2.589	3.965	4.712	5.394	6.121	6.744	7.599
999	2.1236	12.00	1.000	1.000	2.563	3.917	4.625	5.302	5.992	6.593	7.385
Water cloud C1 (13.3 μm)											
300	2.0440	20.00	1.000	1.000	2.627	4.026	4.822	5.499	6.264	6.907	7.833
400	2.0529	20.00	1.000	1.000	2.620	4.014	4.800	5.477	6.234	6.872	7.783
600	2.0716	20.00	1.000	1.000	2.604	3.990	4.755	5.435	6.178	6.807	7.690
999	2.0978	20.00	1.000	1.000	2.585	3.955	4.691	5.368	6.077	6.688	7.520
Water cloud L (5.6 μm)											
300	2.0616	10.00	1.000	1.000	2.613	4.002	4.779	5.458	6.205	6.839	7.735
400	2.0747	10.00	1.000	1.000	2.601	3.984	4.745	5.425	6.158	6.785	7.657
600	2.1005	10.00	1.000	1.000	2.580	3.947	4.679	5.359	6.070	6.684	7.514
999	2.1423	10.00	1.000	1.000	2.545	3.884	4.568	5.244	5.909	6.496	7.250
Ice cloud – hexagonal											
300	2.0000	67.	1.000	1.000	2.435	3.712	4.756	5.960	6.908	7.865	8.954
400	2.0000	67.	1.000	1.000	2.435	3.712	4.756	5.960	6.908	7.865	8.954
600	2.0000	67.	1.000	1.000	2.435	3.712	4.756	5.960	6.908	7.865	8.954
999	2.0000	67.	1.000	1.000	2.435	3.712	4.756	5.960	6.908	7.865	8.954
Ice cloud – irregular											
300	2.0000	50.	1.000	1.000	2.257	3.164	4.096	5.088	6.018	6.897	7.794
400	2.0000	50.	1.000	1.000	2.257	3.164	4.096	5.088	6.018	6.897	7.794
600	2.0000	50.	1.000	1.000	2.257	3.164	4.096	5.088	6.018	6.897	7.794
999	2.0000	50.	1.000	1.000	2.257	3.164	4.096	5.088	6.018	6.897	7.794

Notes:

The different scattering/absorbing media used in Fast-J are tabulated with their relative extinction efficiencies and scattering phase functions as a function of wavelength (λ in nm). Q is the extinction efficiency (cross-section over cross-sectional area), r_{eff} is the mean radius weighted by cross-sectional area, $\bar{\omega}_o$ is the single-scattering albedo (all are assumed conservative here for visible scattering), and ω^0–ω^7 are the first 8 terms in the Legendre expansion of the phase function. The mode radius is the maximum of the number distribution: $r_{mode} = r_{eff}/(1 + 3/\alpha)$. See Table VI for details.

Q and r_{eff} are not used for Rayleigh, isotropic, or absorbing 'soot'.

For stratospheric sulfuric-acid aerosols we use $n = 1.46$ (all wavelengths) and adopt a Log-Normal distribution: $r = 0.09$ μm and $\sigma = 0.6$ for background and $r = 0.08$ μm and $\sigma = 0.8$ for volcanic.

For liquid water clouds we use $n = 1.335$ (all wavelengths) and adopt a Gamma distribution: haze H1 (Deirmendjian, $\alpha = 2$), cloud C1 (Deirmendjian, $\alpha = 6$), and cloud L (Lacis, $\alpha = 11/3$) with the mode radius given (μm). The Lacis Mie parameters are $A = r_{eff}$ and $B = 1/(\alpha + 3)$.

Ice clouds are based on hexagonal or irregular particles (Mishchenko, personal communication). Q and r_{eff} are estimates only, and have no variation with visible wavelength.

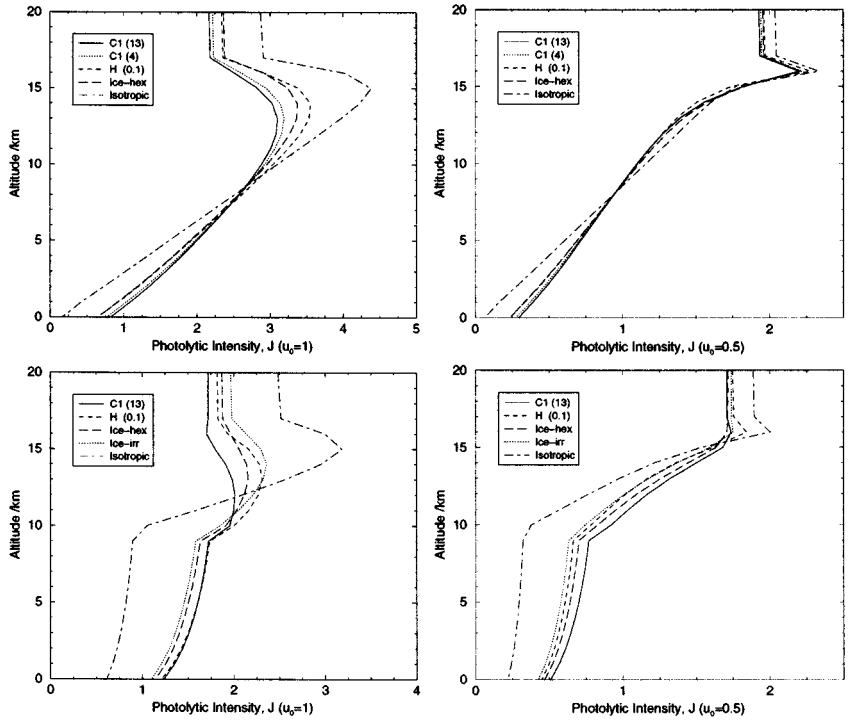

Figure 11. (Top) Photolytic intensity J at 400 nm throughout the atmosphere with a deep cloud of optical depth 20 and different scattering for $\mu_o = 1.0$ (left) and $\mu_o = 0.5$ (right). A background atmosphere with Rayleigh-phase scattering is included with Lambertian surface of albedo 0.1. The cloud is placed uniformly between 1 and 17 km altitude and results are shown from 5 different scattering phase functions: C1 with 13 μm mode radius, C1 with 4 μm mode radius, H1 with 0.1 μm mode radius, hexagonal ice, and isotropic. (Bottom) As above, but with a high cloud of optical depth 4 placed uniformly between 9 and 17 km altitude. Results are shown from 5 different scattering phase functions: C1 with 13 μm mode radius, H1 with 0.1 μm mode radius, hexagonal ice, irregular ice, and isotropic.

clouds, any of the large-particle phase functions in Table VII should give similar results.

The relative photolytic intensity J at 400 nm for a thin (optical depth 4), high cloud (between 9 and 17 km) is shown in Figure 11 (bottom panels) for a range of phase functions. The other conditions of Figure 11 (upper panels) apply. Assuming this to be an ice cloud, the two different ice-cloud phase functions differ by at most 10% with the irregular ice producing larger J in the upper part of the cloud and smaller below the cloud. Once again, isotropic scattering yields large errors throughout the atmosphere. The phase function for liquid water drops (i.e., perfect spheres) is more forward scattering and yields J that is up to 20% smaller throughout most of the ice cloud.

How important are background aerosols? For the optically thick liquid water cloud discussed above (Figure 11), we calculate the impact of background aerosol

on J. It is well known that clouds can enhance the effect of absorbers by increasing the average photon path length. Consider a fully absorbing soot-like aerosol of optical depth 0.01 placed uniformly from 0 to 8 km altitude. For clear sky and overhead sun, this reduces the mean tropospheric J by –1.2% (range from –0.8% to –1.8%). At lower sun angles this effect increases slightly (–1.6%, range from –0.9% to –2.7% at $\mu_o = 0.5$). When a liquid water cloud (C1 at 13 μm) of optical depth 20 is included, the impact of the absorbing aerosol is enhanced by almost a factor of 2 (–2.0%, range from –0.7% to –3.5%) but is still small compared to uncertainties in the phase function or optical depth. Absorption optical depths much greater than 0.01 would be needed to have substantial impacts. Deep clouds have the opposite effect on a background isotropic-like aerosol of optical depth 0.10; they lessen it. In clear sky with overhead sun, the thin isotropic aerosol increases tropospheric J by +4.5% (range from +0.0% to +6.0%). The average impact of such an aerosol with a deep cloud is only +1.0% (range from +0.8% to +2.1%). At lower sun angles, the impact of the thin isotropic aerosol is less, and more ambiguous: Positive in the upper troposphere and negative in the lower. Thus it will be important to include background absorbing aerosols with the clouds for optical depths greater than 0.005, but the impact of background levels of scattering aerosols will be much less important when clouds are present.

C. Optimizing the Integration over Wavelength

Determining photolysis rates requires calculation of the monochromatic photolytic intensity J as a function of wavelength so that the cross section for a given photolysis rate can be weighted by J and integrated over the wavelength region of interest. This need to consider many wavelengths, over which solar flux and cross section may vary considerably, is one of the major computational constraints. The standard UCI photolysis code derived a wavelength quadrature from extremely high-resolution (10 cm^{-1}) data for the solar flux and ozone cross sections. For 'clear-sky' tropospheric photolysis in the 289–850 nm range, the UCI code calculated the optical depth based on ozone absorption and molecular (Rayleigh) scattering. The choice of wavelength bins (quadrature) was made by successively adding 10-cm^{-1} mini-bins from the short-wavelength edge until the photolysis rates of several key species (including ozone) throughout the atmosphere exceeded an error threshold, typically 0.1%, as compared with the 'exact' 10-cm^{-1} calculation made with the 2200 bins from 289 nm to 850 nm. This process continued from the end of the last bin until we had defined 40 large bins. The key to this process is that the average cross section for the large bins must be calculated using the top-of-the-atmosphere solar flux as the weighting kernel. Where high-resolution cross sections for a given species were not available, a spline fit to the tabulated data was used to interpolate to 10 cm^{-1}. This averaging ensures accurate photolysis rates in the optically thin limit, no matter how large the bins. In effect this approach naturally selects wavelength bins over which the solar flux attenuates uniformly

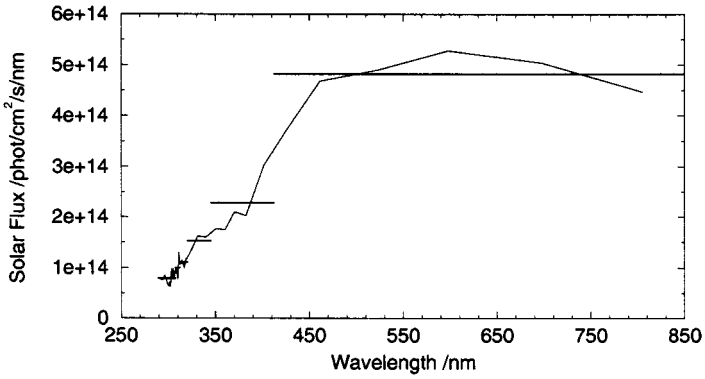

Figure 12. Top-of-atmosphere solar flux (photons cm^{-2} s^{-1} nm^{-1}) for the 40 wavelength bins longward of 289 nm in a standard photolysis calculation (thin line) and the corresponding 7 bins for Fast-J (thick horizontal lines).

throughout the atmosphere. The UCI standard model bin widths range from 1 nm in the 300 nm region to 100 nm at 700 nm, and there are 40 in total.

For the Fast-J scheme, the number of wavelength bins from 289 to 850 nm has been reduced from 40 to 7. The error criteria relative to the standard photolysis scheme was relaxed to 3% over tropospheric altitudes but now included cases with thick clouds as well as clear sky. The grouping of 40 bins into 7 is made objectively by moving the boundaries between the bins until a minimum in the relative root-mean-square errors was achieved for the photolysis rates of O_3 (to $O(^1D)$), NO_2, HNO_3, and H_2O_2. Merging into 6 bins produced unacceptably greater errors, and into 8 bins, no perceptible improvement.

Table VII shows the wavelength bins used for Fast-J, the effective wavelength of each bin, and the corresponding weighted solar flux. The wavelength dependence of the solar flux for the bins is compared with higher-resolution calculations in Figure 12. The table also shows the Fast-J cross sections used for Rayleigh scattering and ozone absorption (at 3 temperatures).

The accuracy of this wavelength quadrature on the calculated photolysis rates of O_3, NO_2 and NO_3 is shown with clear ($\tau = 0$) and cloudy ($\tau = 16$) skies for three different zenith angles (0°, 60° and 80°) in Figure 13. Ozone photolysis (to $O(^1D)$) is barely affected by the quadrature with errors less than 2% even at 60°. Although these relative errors are larger at 80°, the absolute error is still small and has little impact on atmospheric chemistry. The errors for NO_2 photolysis are slightly larger, but still less than 3% at 60°. NO_3 photolysis occurs at the long wavelengths, is represented in Fast-J by a single wavelength bin, and consequently has somewhat larger errors, particularly in the presence of clouds. However, NO_3 photolysis is sufficiently fast that the impact of these errors on atmospheric chemistry is small.

The effects of atmospheric temperature on photolysis rates are included by (1) using temperature-dependent cross sections for the overall absorption of sunlight by ozone, as given in Table VIII, and (2) supplying temperature dependences of the

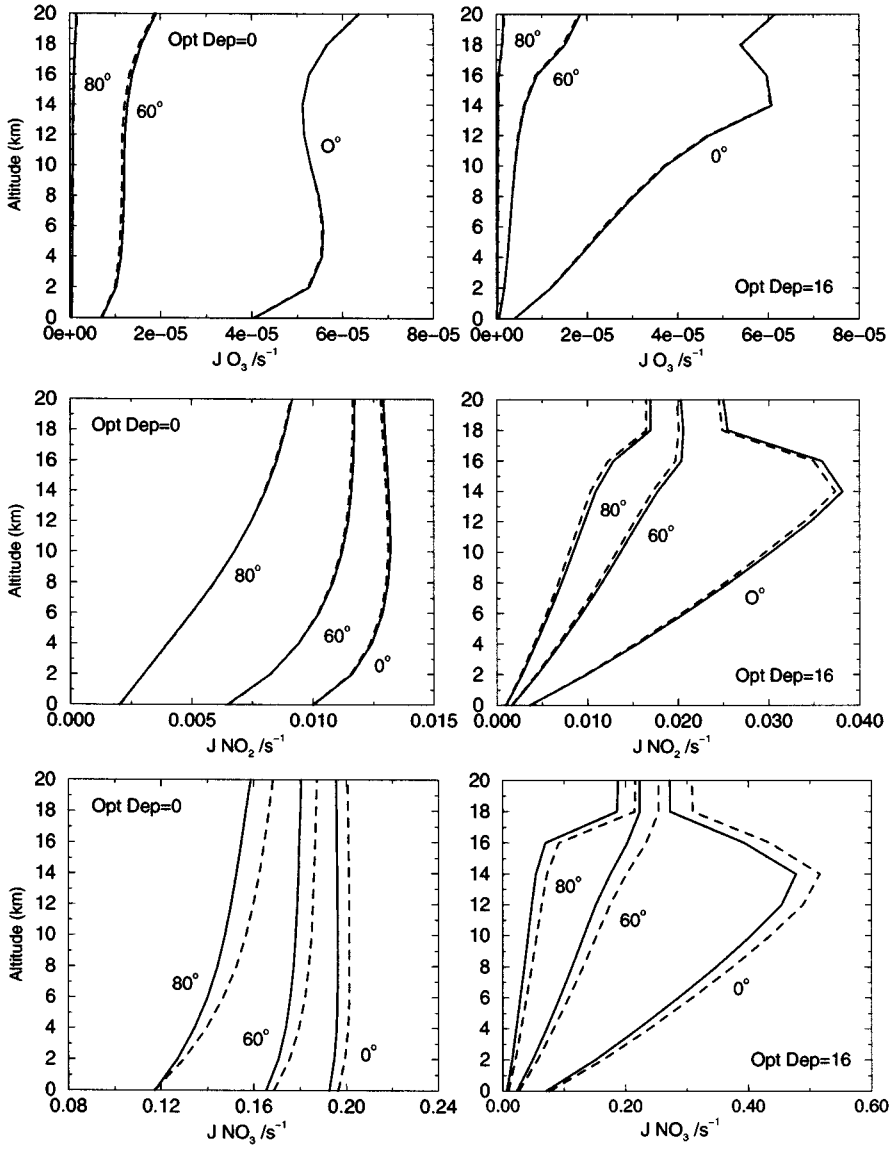

Figure 13. Photolysis rates for O_3 to $O(^1D)$ (top), NO_2 (middle) and NO_3 (bottom) calculated with the 7 Fast-J wavelength bins (solid lines) and with the standard UCI photolysis code using 40 wavelengths (dashed lines). *J*-values were calculated for mid-latitude summer conditions with solar zenith angles of 0°, 60° and 80° for clear sky conditions (left panels) and for a cloud of uniform optical depth 16 through the troposphere (right panels).

Table VIII. Spectral intervals, fluxes and cross-sections for Fast-J

Bin number	1	2	3	4	5	6	7
λ^{Begin} (nm)	289.00	298.25	307.45	312.45	320.30	345.00	412.45
λ^{End} (nm)	298.25	307.45	312.45	320.30	345.00	412.45	850.00
$<\lambda>$ (nm)	294.00	303.00	310.00	316.00	333.00	380.00	574.00
F (10^{14} photons cm^{-2} s^{-1})							
	7.352	7.332	5.022	8.709	37.86	154.4	2110.
$\langle\sigma^{Ray}\rangle$ (10^{-26} cm^2)							
	6.18	5.43	4.92	4.54	3.63	2.09	0.383
$\langle\sigma^{O_3}\rangle$ (10^{-22} cm^2)							
180 K	8693.	2365.	872.2	369.4	42.95	0.1804	16.3
260 K	9189.	2571.	967.3	414.1	54.57	0.2775	16.3
300 K	9574.	2777.	1075.	472.5	67.82	0.4824	16.3
Quantum yield ($O_3 \rightarrow O(^1D)$)							
180 K	0.95000	0.93030	0.30890	0.02290	0.00087	0.00000	0.00000
260 K	0.95000	0.93660	0.46180	0.13800	0.00986	0.00000	0.00000
300 K	0.95000	0.93870	0.53850	0.25240	0.02138	0.00000	0.00000
NO_2							
200 K	1.048E-19	1.494E-19	1.898E-19	2.295E-19	3.391E-19	4.230E-19	4.047E-22
300 K	1.039E-19	1.462E-19	1.845E-19	2.223E-19	3.256E-19	4.150E-19	4.020E-22
$NO_3 \rightarrow NO_2 + O$							
200 K	0.000E+00	0.000E+00	0.000E+00	0.000E+00	0.000E+00	0.000E+00	7.428E-19
298 K	0.000E+00	0.000E+00	0.000E+00	0.000E+00	0.000E+00	0.000E+00	7.428E-19
$NO_3 \rightarrow NO + O_2$							
200 K	0.000E+00	0.000E+00	0.000E+00	0.000E+00	0.000E+00	0.000E+00	9.569E-20
298 K	0.000E+00	0.000E+00	0.000E+00	0.000E+00	0.000E+00	0.000E+00	9.569E-20
HNO_2							
200 K	0.000E+00	0.000E+00	1.265E-20	3.469E-20	1.090E-19	8.644E-20	0.000E+00
300 K	0.000E+00	0.000E+00	1.265E-20	3.469E-20	1.090E-19	8.644E-20	0.000E+00
HNO_3							
200 K	3.706E-21	1.377E-21	5.451E-22	2.102E-22	2.154E-23	8.105E-26	0.000E+00
300 K	4.747E-21	1.923E-21	8.314E-22	3.589E-22	4.764E-23	2.499E-25	0.000E+00
HO_2NO_2							
200 K	2.869E-20	1.102E-20	5.222E-21	2.794E-21	3.255E-22	0.000E+00	0.000E+00
300 K	2.869E-20	1.102E-20	5.222E-21	2.794E-21	3.255E-22	0.000E+00	0.000E+00
PAN							
250 K	2.714E-21	9.251E-22	4.342E-22	2.290E-22	5.508E-23	6.551E-25	0.000E+00
298 K	3.931E-21	1.399E-21	6.730E-22	3.630E-22	9.301E-23	1.193E-24	0.000E+00
H_2O_2							
200 K	8.838E-21	4.991E-21	3.190E-21	2.099E-21	7.716E-22	1.707E-23	0.000E+00
300 K	9.801E-21	5.718E-21	3.773E-21	2.568E-21	1.020E-21	2.287E-23	0.000E+00
$H_2CO \rightarrow HCO + H$							
223 K	0.000E+00	1.969E-20	1.274E-20	1.971E-20	4.354E-21	0.000E+00	0.000E+00
293 K	0.000E+00	1.873E-20	1.304E-20	1.896E-20	3.949E-21	0.000E+00	0.000E+00
$H_2CO \rightarrow CO + H_2$							
223 K	0.000E+00	6.475E-21	4.392E-21	9.027E-21	1.041E-20	1.946E-22	0.000E+00
293 K	0.000E+00	6.163E-21	4.500E-21	8.715E-21	9.434E-21	1.883E-22	0.000E+00

cross sections for the specified photolysis rates. The ozone cross sections plus the quantum yields for $O(^1D)$ are given for 3 temperatures spanning tropospheric values (180 K, 260 K and 300 K). For the other species, temperatures corresponding to the maximum practical range of laboratory measurements are chosen, typically 200 K and 300 K. We use local temperatures to interpolate cross sections linearly and choose not to extrapolate cross sections beyond the measurements. Currently used cross sections for some specific photolysis rates in Fast-J are included in the second part of Table VIII. Cross sections are generally consistent with JPL 97-4 (DeMore *et al.*, 1997).

References

Anderson, D. E., Demajistre, R., Lloyd, S. A., and Swaminathan, P. K., 1995: Impact of aerosols and clouds on the troposphere and stratosphere radiation-field with application to twilight photochemistry at 20 km, *J. Geophys. Res.* **100**, 7135–7145.

Atkinson, R., Baulch, D. L., Cox, R. A., Hampson, R. F., Kerr, J. A., Rossi, M. J., and Troe, J., 1997: Evaluated kinetic, photochemical and heterogeneous data for atmospheric chemistry, Supplement V – IUPAC Subcommittee on Gas Kinetic Data Evaluation for Atmospheric Chemistry, *J. Phys. Chem. Ref. Data* **26**, 521–1011.

Auer, L., 1967: Improved boundary conditions for the Feautrier method, *Astrophys. J.* **150**, 53–55.

Berntsen, T. K. and Isaksen, I. S. A., 1997: A global three-dimensional chemical transport model for the troposphere. 1. Model description and CO and ozone results, *J. Geophys. Res.* **102**, 21239–21280.

Brasseur, G. P., Hauglustaine, D. A., Walters, S., Rasch, P. J., Muller, J.-F., Granier, C., and Tie, X. X., 1998: MOZART, a global chemical tracer model for ozone and related chemical tracers. 1. Model description, *J. Geophys. Res.* **103**, 28265–28289.

Brock C. A., Jonsson, H. H., Wilson, J. C., Dye, J. E., Baumgardner, D., Borrmann, S., Pitts, M. C., Osborn, M., Decoursey, R. J., and Woods, D. C., 1993: Relationships between optical extinction, backscatter and aerosol surface and volume in the stratosphere following the eruption of Mt Pinatubo, *Geophys. Res. Lett.* **20**, 2555–2558.

Boucher, O., Schwartz, S. E., Ackerman, T. P., Anderson, T. L., Bergstrom, B., Bonnel, B., Chylek, P., Dahlback, A., Fouquart, Y., Fu, Q., Halthore, R. N., Haywood, J. M., Iversen, T., Kato, S., Kinne, S., Kirkevag, A., Knapp, K. R., Lacis, A., Laszlo, I., Mishchenko, M. I., Nemesure, S., Ramaswamy, V., Roberts, D. L., Russell, P., Schlesinger, M. E., Stephens, G. L., Wagener, R., Wang, M., Wong, J., and Yang, F., 1998: Intercomparison of models representing direct shortwave radiative forcing by sulphate aerosols, *J. Geophys. Res.* **103**, 16979–16998.

Cameron-Smith, P. J., 2000 (this issue): Incorporation of non-linear cross-section parameterizations into a fast photolysis computation code (Fast-J), *J. Atmos. Chem.* **37**, 283–297.

Chandrasekhar, S., 1960: *Radiative Transfer*, Dover, New York, p. 393.

Chang, J. S., Brost, R. A., Isaksen, I. S. A., Madronich, S., Middleton, P., Stockwell, W. R., and Walcek, C. J., 1987: A three-dimensional Eulerian acid deposition model: Physical concepts and formulation, *J. Geophys. Res.* **92**, 14681–14700.

Cochran, W. D. and Trafton, L. M., 1978: Raman scattering in the atmospheres of the major planets, *Astrophys. J.* **219**, 756–762.

Dave J. V. and Armstrong, B. H., 1970: Computation of high-order associated Legendre Polynomials, *J.Q.S.R.T.* **10**, 557–562.

Deirmendjian, D., 1969: *Electromagnetic Scattering on Spherical Polydispersions*, American Elsevier, New York, p. 287.

DeMore, W. B., Sander, S. P., Golden, D. M., Hampson, R. F., Kurylo, M. J., Howard, C. J., Ravishankara, A. R., Kolb, C. E., and Molina, M. J., 1997: Chemical kinetics and photochemical data for use in stratospheric modeling, JPL Publication, 97-4, Jet Propulsion Lab., Pasadena.

Feautrier, P., 1964: *Comptes Rendues* **258**, 3189–3199.

Goody, R. M. and Yung, Y. L., 1989: *Atmospheric Radiation*, Oxford University Press, New York, p. 519.

Hansen, J. E. and Travis, L., 1974: Light scattering in planetary atmospheres, *Space Sci. Rev.* **16**, 527–610.

Henyey, L. C. and Greenstein, J. L., 1941: Diffuse radiation in the galaxy, *Astrophys. J.* **93**, 70–83.

Hough, A. M., 1988: The calculation of photolysis rates for use in global tropospheric modelling studies, AERE Report R-13259, H.M. Stationery Office, London.

Isaksen, I. S. A., Midtbo, K. H., Sunde, J., and Crutzen, P. J., 1977: A simplified method to include molecular scattering and reflection in calculations of photon fluxes and photodissociation rates, *Geophys. Norv.* **31**, 11–26.

Jacob, D., Gottlieb, E., and Prather, M. J., 1989: Chemistry of a polluted cloudy boundary layer, *J. Geophys. Res.* **94**, 12975–13002.

Joseph, J. H., Wiscombe, W. J., and Weinman, J. A., 1976: The delta-Eddington approximation for radiative flux transfer, *J. Atmos. Sci.* **33**, 2452–2459.

Kraus, A. B., Rohrer, F., Grobler, E. S., and Ehhalt, D. H., 1996: The global tropospheric distribution of NO_x estimated by the three-dimensional chemical tracer model, *J. Geophys. Res.* **101**, 18587–18604.

Kylling, A., Stamnes, K., and Tsay, S. C., 1995: A reliable and efficient two-stream algorithm for spherical radiative transfer: Documentation of accuracy in realistic layered media, *J. Atmos. Chem.* **21**, 115–150.

Landgraf, J. and Crutzen, P. J., 1998: An efficient method for online calculations of photolysis and heating rates, *J. Atmos. Sci.* **55**, 863–878.

Liao, H., Yung, Y. L., and Seinfeld, J. H., 1999: Effects of aerosols on tropospheric photolysis rates in clear and cloudy atmospheres, *J. Geophys. Res.* **104**, 23697–23707.

Liousse, C., Penner, J. E., Chuang, C., Walton J. J., Eddleman, H., and Cachier, H., 1996: A global three-dimensional model study of carbonaceous aerosols, *J. Geophys. Res.* **101**, 19411–19432.

Logan, J. A., Prather, M. J., Wofsy, S. C., and McElroy, M. B., 1981: Tropospheric chemistry: A global perspective, *J. Geophys. Res.* **86**, 7210–7254.

Madronich, S., 1987: Photodissociation in the atmosphere: 1. Actinic flux and the effects of ground reflections and clouds, *J. Geophys. Res.* **92**, 9740–9752.

Michelangeli, D. V., Allen, M., Yung, Y. L., Shia, R. L., Crisp, D., Eluszkiewicz, J., 1992: Enhancement of atmospheric radiation by an aerosol layer, *J. Geophys. Res.* **97**, 865–874.

Mishchenko, M. I., Rossow, W. B., Macke, A., and Lacis, A. A., 1996: Sensitivity of cirrus cloud albedo, bidirectional reflectance and optical thickness retrieval accuracy to ice particle shape, *J. Geophys. Res.* **101**, 16973–16985.

Müller, J. F. and Brasseur, G., 1995: IMAGES: A three-dimensional chemical transport model of the global troposphere, *J. Geophys. Res.* **100**, 16445–16490.

Olsen, J., Prather, M., Berntsen, T., Carmichael, G., Chatfield, R., Connell, P., Derwent, R., Horowitz, L., Jin, S., Kanakidou, M., Kasibhatla, P., Kotamarthi, R., Kuhn, M., Law, K., Penner, J., Perliski, L., Sillman, S., Stordal, F., Thompson, A., and Wild, O., 1997: Results from the Intergovernmental Panel on Climate Change photochemical model intercomparison (PhotoComp), *J. Geophys. Res.* **102**, 5979–5991.

Penner, J. E., Dickinson, R. E., and O'Neill, C. A., 1992: Effects of aerosol from biomass burning on the global radiation budget, *Science* **256**, 1432–1433.

Prather, M. J., 1974: Solution of the inhomogeneous Rayleigh scattering atmosphere, *Astrophys.J.* **192**, 787–792.

Prather, M., McElroy, M., Wofsy, S., Russell, G., and Rind, D., 1987: Chemistry of the global troposphere: Fluorocarbons as tracers of air motion, *J. Geophys. Res.* **92**, 6579–6613.

Prather, M. J. and Remsberg, E. E. (eds), 1993: The atmospheric effects of stratospheric aircraft: Report of the 1992 stratospheric models and measurements workshop, NASA Ref. Publ., 1292, p. 672.

Quinn, P. K., Kapustin, V. N., Bates, T. S., and Covert, D. S., 1996: Chemical and optical properties of marine boundary layer aerosol particles of the mid-Pacific in relation to sources and meteorological transport, *J. Geophys. Res.* **101**, 6931–6951.

Rind, D. and Lerner, J., 1996: Use of on-line tracers as a diagnostic tool in general circulation model development: 1. Horizontal and vertical transport in the troposphere, *J. Geophys. Res.* **101**, 12667–12683.

Roelofs, G. J. and Lelieveld, J., 1995: Distribution and budget of O_3 in the troposphere calculated with a chemistry general circulation model, *J. Geophys. Res.* **100**, 20983–20998.

Rossow, W. B. and Schiffer, R. A., 1991: ISCCP cloud data products, *Bull. Amer. Meteor. Soc.* **72**, 2–20.

Schimel, D. *et al.*, 1996: Radiative forcing of climate, in J. T. Houghton *et al.* (eds), *Climate Change, 1995 – The Science of Climate Change* (Chapter 2), Cambridge University Press, New York, pp. 65–131.

Spivakovsky, C. M., Logan, J. A., Montzka, S. A., Balkanski, Y. J., Foreman-Fowler, M., Jones, D. B. A., Horowitz, L. W., Fusco, A. C., Brenninkmeijer, C. A. M., Prather, M. J., Wofsy, S. C., and McElroy, M. B., 2000: Three-dimensional climatological distribution of tropospheric OH: Update and evaluation, *J. Geophys. Res.* **105**, 8931–8980.

Stamnes, K., Tsay, S. C., Wiscombe, W., and Jayaweera, K., 1988: Numerically stable algorithm for discrete-ordinate method radiative transfer in multiple scattering and emitting layered media, *Applied Optics* **27** (12), 2502–2509.

Tegen, I. and Fung, I., 1995: Contribution to the atmospheric mineral dust load from land surface modification, *J. Geophys. Res.* **100**, 18707–18726.

Thekeakara, M. P., 1974: Extra-terrestrial solar spectrum, 3000–6100 A at 1 A intervals, *Appl. Opt.* **13**, 518–522.

van de Hulst, H. C., 1981: *Light Scattering by Small Particles*, Dover, New York, p. 471.

Wild, O. and Prather, M. J., 2000: Excitation of the primary tropospheric chemical mode in a global 3-D model, *J. Geophys. Res.*, accepted.

Wilson J. C., Jonsson, H. H., Brock, C. A., Toohey, D. W., Avallone, L. M., Baumgardner, D., Dye, J. E., Poole, L. R., Woods, D. C., Decoursey, R. J., Osborn, M., Pitts, M. C., Kelly, K. K., Chan, K. R., Ferry, G. V., Loewenstein, M., Podolske, J. R., and Weaver, A., 1993: In-situ observations of aerosol and chlorine monoxide after the 1991 eruption of Mount Pinatubo – effect of reactions on sulfate aerosol, *Science* **261**, 1140–1143.

Wiscombe, W. J., 1977: The delta-M method: Rapid yet accurate radiative flux calculations for strongly asymmetric phase functions, *J. Atmos. Sci.* **34**, 1408–1422.

World Meteorological Organisation, 1986: Atmospheric Ozone 1985: Assessment of our understanding of the processes controlling its present distribution and change, Global Ozone Research and Monitoring Project, Report 16.

Zeng, J., Madronich, S., and Stamnes, K., 1996: A note on the use of the two-stream delta-scaling approximation for calculating atmospheric photolysis rate coefficients, *J. Geophys. Res.* **101**, 14525–14530.